This is to certify that the

dissertation entitled

Non-Equilibrium Proximity Effect
In a SNS Junction

presented by

JIAN HUANG

has been accepted towards fulfillment
of the requirements for

Ph D degree in Physics

Norman O. Birge

Major professor
N. Birge

Date December 10, 2001

NON-EQUILIBRIUM PROXIMITY EFFECT IN A SNS Junction

By

JIAN HUANG

A DISSERTATION

Submitted to
Michigan State University
in partial fulfillment of the requirements
for the degree of

DOCTOR OF PHILOSOPHY

Physics

2001

ABSTRACT
NON-EQUILIBRIUM PROXIMITY IN JOSEPHSON DEVICE
By
JIAN HUANG

Our goal is to study the quasiparticle-induced nonequilibrium proximity effect in a SNS device. We first performed a dangling arm experiment which demonstrates the counter-flowing quasiparticle current and supercurrent. Then, a second experiment was performed to demonstrate the appearance of a π junction. Baselmans et al. [1] have recently shown that the direction of the supercurrent in a superconductor/normal/superconductor Josephson junction can be reversed by applying, perpendicularly to the supercurrent, a sufficiently large control current between two normal reservoirs. The novel behavior of their 4-terminal device (called a controllable π-junction) arises from the nonequilibrium electron energy distribution established in the normal wire between the two superconductors. We have observed a similar supercurrent reversal in a 3-terminal device, where the control current passes from a single normal reservoir into the two superconductors. We show theoretically that this behavior, although intuitively less obvious, arises from the same nonequilibrium physics present in the 4-terminal device. The difference lies in the scattering of the Cooper pair states by quasiparticles with zero momentum (Baselmans') and with a finite momentum (our device). Moreover, we argue that the amplitude of the π-state critical current should be at least as large in the 3-terminal device as in a comparable 4-terminal device.

To God Who is loving and merciful

and

To my dearest wife and daughter

ACKNOWLEDGEMENTS

I would like to thank my advisor, Professor Norman Birge, for his constant support and care for the past four years. For this work would have been impossible without him. I really appreciate this opportunity of working with him and it has been a tremendous experience. I enjoy many things I have learned from him and I have always found encouragement through various things we worked on together.

My thanks go to Professor Mahanti, Professor Phil Duxbery, Professor Mark Dykman, and Professor Zelevinsky for many enlightening discussions with them. Their knowledge on many subjects will always encourage and spur me for better work. I would like to thank Professor V. Ambegaokar, J. Saul and Professor Abrikosov for their teaching on superconductivity and Green's functions which brings better understanding. My thanks go to Professor C. Lobb and D. Ralph for their comments on the metal-metal contact issues. Thanks to Frank Wilhelm for many explanations of the quasiclassical theory. I would like to thank Dr. Baokang Bi for his generosity and patience in teaching me the fabrication techniques. My thanks go to H. Pothier and D. Esteve at Saclay group for their support and insights. I want to thank Fred Pierre for his help with the experiment and many discussions. My thanks go to Reza Loloee for his help with the SQUID measurement. My deep appreciation also goes to Prefessor I. O. Kulik who shared key ideas for our experiment. I also extend my thanks to Professor Volkov for a helpful comment regarding the theoretical calculations.

This work is supported by the National Science Foundation (grants DMR-9801841 and DMR-0104178) and the Keck Microfabrication Facility.

Table of Contents

LIST OF TABLES ix

LIST OF FIGURES x

1 Introduction 1

1.1 Background 1

1.2 Motivation 2

2 Review 6

2.1 From Simple Metal to Superconductor 6

2.1.1 Dielectric Function 6

2.1.2 BCS Theory 10

2.2 NS System 11

2.2.1 Modified States at the NS interface and Bogolubov- de Gennes Equation 11

2.2.2 Andreev Reflection 14

2.2.3 Proximity Effect 16

2.3 SNS Josephson Effect and Andreev Bound States 18

2.4 Spectral Supercurrent Density 19

2.4.1 Ballistic case 20

2.4.2 Diffusive case 21

2.5 Distribution Functions 22

2.6 π Junction 25

2.7 Summary 27

3 Fabrication Methods **29**

3.0.1 Surface Preparation 29

3.1 Photolithograhy 30

3.1.1 Photo Resist Coating 30

3.1.2 Photo Resist Baking 32

3.1.3 Exposure 32

3.1.4 Development 33

3.1.5 Evaporation and Liftoff 33

3.1.6 Photo-alignment 34

3.2 Electron Beam Lithography (EBL) 34

3.2.1 Electron-Solid Interaction and Proximity Effect 36

3.2.2 Electron Beam Writing 39

3.2.3 Development 40

3.2.4 Electron Beam Alignment 40

3.3 Actual Sample Making 43

3.3.1 Review of Methods 43

3.3.2 Method 1: E-beam First, Photolithography Second 45

3.3.3 Method 2: Photolithography First, E-beam Second 49

4 Electronics for Measurement **52**

4.1 Sample Mounting 52

4.2 Electronics 52

4.2.1 DC Measurement 55

4.2.2 AC Measurement 55

5 First Experiment: Dangling Arm **57**

5.1 DC and AC Measurement between the N and S Terminals 58

5.2 DC and AC Measurement between the S and S Terminals 60

5.2.1 Analysis 60

5.3 Temperature Dependence 63

5.4 Summary 64

6 π-Junction **65**

6.1 Observation of the π-Junction 65

6.1.1 Experiment 65

6.1.2 Discussion on the appearance of π junction 69

6.2 π-Junction affected by the rounding of f_0 70

6.2.1 Temperature 70

6.2.2 e^-e^- interaction 71

6.3 Comparison with Baselmans' Experiment 75

6.4 Sub-harmonic Gap Structure 78

7 Quasiclassical Theory **80**

7.1 Review of the quasiclassical formalism 80

7.2 Analytical Solution with High-barrier Approximation 87

Appendices **94**

A Tunnel Junctions **95**

B High Barrier ($R_b >> R_N$) Approximation **97**

C Diffusive region **99**

LIST OF REFERENCES **101**

List of Tables

3.1 Metal deposition current and rate for Edward Auto306 thermal evaporator 34

3.2 3-level alignment 41

3.3 Spin and baking conditions for $7mm \times 7mm$ Si substrate 46

3.4 E-beam writing conditions for single path 47

3.5 E-beam resist Development 47

3.6 Thermal evaporation of the nanowire 47

3.7 photo printing condition 48

3.8 Thermal evaporation of Silver reservoir 48

3.9 Ion-milling 48

5.1 Experimental results vs. prediction 58

List of Figures

1.1 Schematic of Sample and measurement circuit 2

1.2 Two current flow regimes 2

1.3 Expected V vs. I for dangling arm experiment 3

1.4 Schematic picture of the measurement with varied normal injection . 4

1.5 Schematic picture of the expected V-I measurement corresponding to a π junction at large values of injected current I_{inj} 5

2.1 Schematic picture of a metal 7

2.2 Schematic picture of Andreev reflection 14

2.3 Schematic picture of the proximity effect 16

2.4 Schematic picture of the Andreev bound states formed in a SNS long junction with $L < L_\phi$ 18

2.5 Energy levels of the excitations in the normal region at a fixed value of electron velocity [2] 20

2.6 Spectral supercurrent density vs. excitation energy for different phase differences for a 3-terminal superconductor-semiconductor-superconductor device [3] 21

2.7 Calculated spectral supercurrent density by quasiclassical approach. The units for energy is meV 22

2.8 Distribution functions for different sample lengths for N-n-N structures. Upper right: $L > L_{e-ph}$; lower left: $L_{e-e} < L < L_{e-ph}$; lower right: $L < L_{e-e}, L_{e-ph}$ [4] 23

2.9 A S-n-N system with N elevated by voltage V 24

2.10 A schematic picture of how a quasiparticle distribution function varies in space. The solid dot stand for an particle and the circle stands for an Andreev reflected hole. The size of the circles stand for the amplitude of distribution function of the particle/hole 24

2.11 A schematic picture of the distribution function with correction due to both temperature and proximity effects 25

2.12 Antisymmetric distribution function f_0 (upper graph) and the spectral supercurrent density 27

3.1 A schematic picture of photo printing 32

3.2 E-beam Process: (a) Spin-coat the substrate with e-beam resist. Expose the resist with electron beam. (b) Develop the resist. (c) Metal deposition. (d) After lift-off 35

3.3 Block diagram showing the major components of a typical electron beam lithography system 35

3.4 Simulated profile of the energy absorbed from an electron beam exposure [5] 37

3.5 SEM pictures of a series of single paths (Ag lines) with following doses in nC/cm: 2.0, 2.1, 2.2, 2.3, 2.4, 2.5, 2.6, 2.7, and 2.8. 39

3.6 Width of the single path versus dose 40

3.7 Schematics of an angle evaporation method. The two sets of patterns are from evaporations at different angles 44

3.8 Three Steps of making the the sample 46

3.9 SEM pictures of the sample. The upper picture was taken at 10kX and the lower picture was taken at 18kX 50

3.10 The dimensions of the actual sample 51

3.11 SEM picture (taken at 20kX) of the sample by method 2 51

4.1 Schematics of the sample holder 53

4.2 Schematics of the sample mounting 53

4.3 electronic setup for the DC measurement 54

4.4 Electronic setup for ac measurement 56

5.1 SEM picture of the sample 57

5.2 DC measurement of V-I 58

5.3 AC measurement of (dV/dI) vs. I 59

5.4 DC measurement between the superconducting terminals 60

5.5 AC measurement between the superconducting terminals 61

5.6 Temperature dependence of the critical currents $I_C(SN)$ and $I_C(SNS)$ 63

6.1 SEM picture of the sample and the measurement circuit. The picture is take at 10kX. The distance between S terminals is 1.1μm, and the distance between the cross point and N terminal(bottom of the picture) is 4.5μm 65

6.2 dc measurement of the V-I characteristics for different values of I_N . 66

6.3 Selected curves from the previous graph for following values of I_N: 0.53, 0.70, 1.01, 1.23, 1.89, 2.18, 3.15 μA 67

6.4 $I_C(SNS) vs. I_{inj}$ at 40 mK 67

6.5 I_C vs. V_{inj} 68

6.6 Absence of the π junction resulted from the rounding of the distribution function due to the increase of temperature 71

6.7 V-I characteristics for 96mK, 200mK, and 304mK 72

6.8 I_C vs. I_{inj} and I_C vs. V_{inj} for 96mK, 200mK, and 304mK 73

6.9 Schematic picture of Baselmann's four terminal device and measurement setup [1] 75

6.10 Observed π junction and I_C vs. $V_{control}$ in Baselmans et al's experiment [1] 76

6.11 Difference of changes of $R_{eff}(SN)$ at zero phase state and π state . . 76

6.12 Comparison of the total distribution functions between baselmans' device (top) and a four-terminal device with current flow equivalent to that in our device (bottom) 77

6.13 Schematic picture of multi-Andreev processes 78

6.14 Observation of the Sub-harmonic Gap Structure 79

7.1 The diagram equation for Green's functions 82

7.2 Comparison of the experiment and theory for $I_C(SNS)$ vs. T for the dangling arm case 90

7.3 Experimental data for $I_C(SN)$ vs. T for the dangling arm case 91

7.4 Theoretical calculations of I_+, I_-, and I_C at 40 mK 92

7.5 Comparison of the $Im[j(E)]$ vs. V_{inj} from the numerical calculation and the high-barrier approximation for the π junction case 92

7.6 Comparison of I_C vs. V_{inj} between the theory and experiment for the π junction case 93

B.1 SNS system 97

Chapter 1: Introduction

1.1 Background

The study of normal conductor-superconductor systems first started in the 60's. The phenomenon of superconductivity is a remarkable example of quantum effect operating on a truly macroscopic scale, while the macroscopic properties of normal metal are rather classical. Only when the normal metal is made mesoscopic, quantum phenomena are found on a scale of the phase-coherence-length L_ϕ. The proximity effect was first studied within the framework of Ginzburg-Landau [6] in which the superconducting order is expressed by a complex order parameter $\Psi(r)$ which is related to the pair correlations. Later, a more rigorous treatment was done by using Bogoliubov-de Gennes equations (BdG) [7], where the eigenstates describe the electron-like and hole-like excitations. It was understood then that proximity effect describes the phenomenon where the superconducting order can extend far into the normal region even in absence of the attractive potential between the electrons. Since the 1990's, there has been a revival of interest in studying the proximity effect, which started with bringing together superconductivity and mesoscopic physics (Altshuler et al 1991 [8]). Meanwhile, modern fabrication techniques enable us to make devices with sub-micrometer dimensions. The first experiment that measured the phase coherent transport properties in submicron superconductor devices were performed by Petrashov and Antonov [9] (1991) and Kastalskii et al [10] (1991). Since then, there have been active studies in understanding the physics as well as applications. The significant progress made during the past ten years or so signals that the seed planted 30 years ago is growing into a rich field of study. As a result of much work, the equilibrium proximity effect is well understood now. But, nonequilibrium situations are still under investigation.

1.2 Motivation

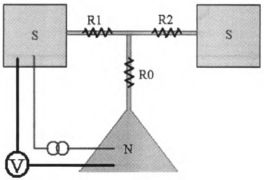

Figure 1.1: Schematic of Sample and measurement circuit

We are particularly interested in studying the non-equilibrium transport phenomena in a long superconductor-normal metal-superconductor(SNS) junction (in the diffusive regime) where the nonequilibrium is introduced by injecting quasiparticle current from a normal reservoir. We considere the system shown in figure 1.1. It is a SNS long junction with an extra normal lead connected to the middle of the normal wire to inject quasiparticle current. If a normal current is driven from the normal reservoir to one of the superconducting(SC) reservoirs, the peaceful equilibrium is destroyed. Despite the fact that there are complicated microscopic changes, the system will respond in one of the following two ways illustrated in figure 1.2.

If the current goes directly into the left SC reservoir, a potential difference is

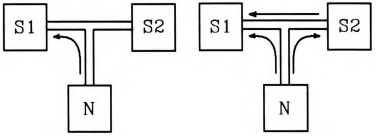

Figure 1.2: Two current flow regimes

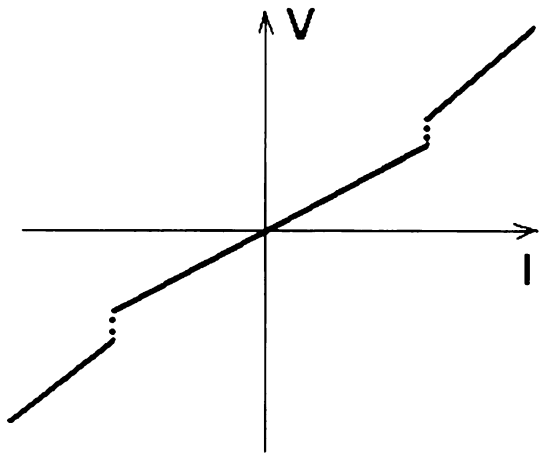

Figure 1.3: Expected V vs. I for dangling arm experiment

created between the SC reservoirs. There arises an ac Josephson current due to this finite voltage difference. The effective resistance between the N reservoir and the left SC reservoir is simply $R_{eff} = R_0 + R_1$. We believe this is what happens when the driving current exceeds a certain critical current. At an injection current smaller than the critical current, the dc Josepshon effect may take place. The normal current can split at the cross point going into both SC reservoirs so that the voltage drops from the cross point to the two SC reservoirs are the same. To satisfy the Kirchhoff's law, a dc Josephson current arises going from right to left so that the total current in the right arm is zero. The SC reservoirs are as if tied together. The effective resistance between the N reservoir and the left SC reservoir is then $R_{eff} = R_0 + R_1//R_2$. So, we expect a V-I relationship like the one shown in figure 1.3. If we indeed see this type of V-I curve, we will know that when $I < I_C$, there are counter-flowing quasiparticle current and supercurrent in the dangling arm.

We also performed a second measurement (shown in Figure 1.4) where we drive the system farther away from equilibrium to see if a π junction appears by controlling the normal current injection. We also aimed to understand if the same physics appears studied by Baselmanns et al [1]. Unlike the dangling arm situation, this experiment does not have the constraint that $2I_S \cong I_N$. This means the driving

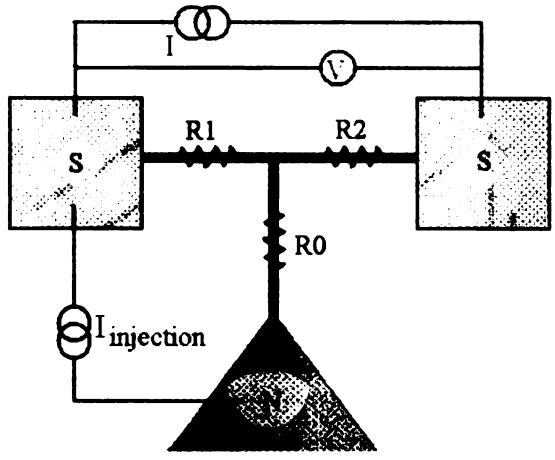

Figure 1.4: Schematic picture of the measurement with varied normal injection

current can be much higher than the critical current I_C before the dc Josephson effect goes away. The condition for a π junction is that the distribution function of the quasiparticles inside the normal region has a staircase shape. We fabricated our sample so that the length of the normal region is smaller than the phase breaking length L_ϕ, so that there is little energy exchange among the electrons. We also fabricated thick normal reservoir (220nm thick) to ensure efficient electron-phonon interaction to avoid heating. Thus, the staircase distribution function is achieved. We measured the V-I characteristics between the two SC reservoirs with different values of normal injection. The V-I characteristics should be like those shown in figure 1.5, where the critical current shrinks first as the injection increases, goes to zero at a certain point, then, opens up again, then goes to zero eventually. If we see this type of data, we know the π junction has occurred.

By comparing our data with the quasiclassical theory, we want to evaluate, as the sample goes further away from equilibrium, if the electron-electron interaction becomes an important factor.

There are some lengths involved in characterizing the transport properties. They are defined as following:

Fermi wave length λ_F

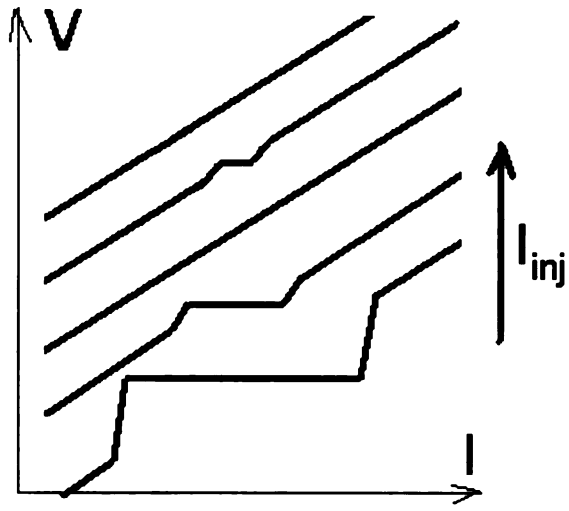

Figure 1.5: Schematic picture of the expected V-I measurement corresponding to a π junction at large values of injected current I_{inj}

Phase breaking length L_ϕ is a characteristic length for the interference of the electron wave functions. It is a length on which a wave packet can travel without loosing its phase coherence.

Thermal Length: L_T is also called normal conductor phase coherence length. It is a length on which quasiparticles lose phase coherence.

Correlation Length for proximity effect $L_E = \sqrt{\hbar D/2E}$ is an energy-dependent length scale on which the Cooper-pair-like states lose phase coherence.

Chapter 2: Review

This chapter starts with introducing the nature of the attractive potential between the electrons through the dielectric function with both electron-electron repulsion and electron-phonon interaction. Then, BCS theory, based on the attractive potential between the partners inside a Cooper pair, is reviewed. Then, in discussing modified states of NS systems, the four-fold degenerate states in the normal region, a result of solving the Bogoliubov-de Gennes equation, is presented. This lays the ground work for the next discussion of Andreev reflection and proximity effect. Then, the proximity effect in long SNS junctions is discussed with the language of Andreev bound states. This is followed by more in-depth discussion of spectral supercurrent density (energy spectrum of the system) and the distribution function (occupation of the energy states). Then, π junction is explained in terms of spectral supercurrent density and antisymmetric distribution function. The chapter ends with a brief summary of current theoretical approaches.

2.1 From Simple Metal to Superconductor

2.1.1 Dielectric Function

[Note: the derivations below are inspired by Ambegaokar's notes on review of superconductivity[11]]

In a simple metal shown in figure 2.1, the basic ingredients of the interactions are:

- e^- in periodic potential + Coulomb repulsion
- Ions + Ion-Ion interaction $\rightarrow$ phonons
- e^--phonon interaction

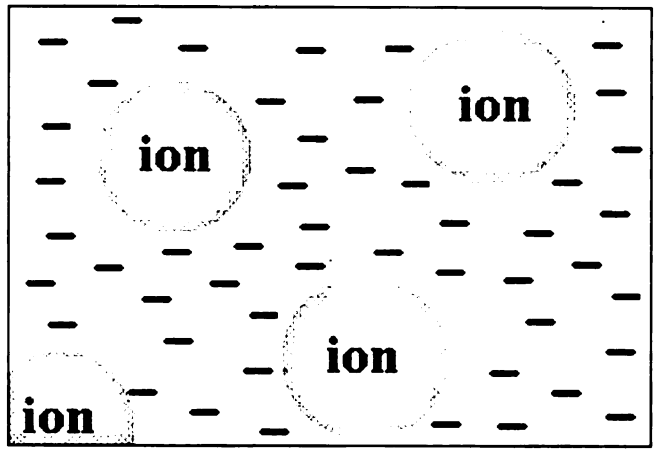

Figure 2.1: Schematic picture of a metal

- Impurities

Despite the strong interaction among the electrons, the system is reasonably described by the independent-particle model. This is based on the fact, traced by Landau [12], that single particle excitations obey Fermi-Dirac statistics and the number of the excitations is small at normal temperature. These independent particles are called quasipariticles which are the basic bricks of Fermi-liquid theory.

When in the superconducting phase, the electron-phonon interaction, as Frohlich [13] pointed out, mediates the electron-electron interaction. Now, let's look at the dielectric function in the presence of both e-e repulsion and e-phonon interaction. For an electronic system, at sufficiently long wavelengths or at frequencies $\omega \ll \omega_{pl} = \sqrt{4\pi ne^2/m}$, we have

$$\vec{j} = -eD\vec{\nabla}n - \sigma\vec{\nabla}\phi \approx -eD\frac{\partial n}{\partial \mu}\vec{\nabla}\mu - \sigma\vec{\nabla}\phi \tag{2.1}$$

where D is the diffusion constant, e is the charge, σ is the conductivity, and ϕ is the electric potential. In equilibrium, $\mu + e\phi = constant$, and $j = 0$, which leads to the Einstein relation

$$\sigma = e^2 \frac{\partial n}{\partial \mu} D \tag{2.2}$$

If we plug 2.1 into the charge conservation $e\partial n/\partial t + \nabla \cdot j = 0$, we have

$$\frac{\partial n}{\partial t} = D\nabla^2 n + 2N(0)De\nabla^2 \phi \tag{2.3}$$

where $\partial n/\partial \mu = 2N(0)$ ($N(0)$ is the density of states per spin). Now, $\nabla^2 \phi = 4\pi \rho_T$ where $\rho_T = \rho_{ext} + ne$ is the total charge. The Fourier transformation of the equation above gives

$$(i\omega + Dq^2)en(q,\omega) = -8\pi N(0)e^2 D\rho_T \equiv -k_s^2 D\rho_T \tag{2.4}$$

where $k_s^2 = 8\pi N(0)e^2$. The dielectric function is defined by $\epsilon \rho_T = \rho_{ext}$ which can also be written as

$$en(q,\omega) = [\frac{1}{\epsilon(q,\omega)} - 1]\rho_{ext}(q,\omega) \tag{2.5}$$

Thus, we have the dielectric constant with the correction of the screening of the electrons

$$\epsilon(q,\omega) \cong 1 + \frac{k_s^2}{-i\omega/D + q^2} \tag{2.6}$$

for $q \ll k_F$ and $\omega \ll \omega_{pl}$. Now, we also need to include phonons. For the unscreened ions,

$$\frac{\partial j_{ion}}{\partial t} = -\frac{n_{ion}(Ze)^2}{M} \nabla \phi \tag{2.7}$$

where -Ze is the ion charge, M is ion mass, and n_{ion} is ion density. Again, following the similar derivation with charge conservation as that for electrons shown above, one obtains $\epsilon = 1 - \Omega_{ph}^2/\omega^2$ where $\Omega_{ph}^2 = 4\pi n_{ion}(Ze)^2/M$. Then, the total dielectric function is roughly

$$\epsilon(q,\omega) \cong 1 + \frac{k_s^2}{-i\omega/D + q^2} - \frac{\Omega_{ph}^2}{\omega^2} \tag{2.8}$$

Coulomb forces thus screen longitudinal phonons and electron-electron interactions. If we ignore the $-i\omega/D$ correction (low frequencies), the screened interaction is roughly

$$\frac{4\pi e^2}{q^2\epsilon(q,\omega)} = \frac{4\pi e^2}{q^2 + k_s^2}[1 + \frac{\Omega_{ph}^2/\omega^2}{q^2 + k_s^2 - \Omega_{ph}^2/\omega^2}] \tag{2.9}$$

Screened Coulomb repulsion plus exchange of screened longitudinal phonons becomes attractive at low frequencies. Though the repulsion and the attraction are both short-ranged, they work at different band width: The attraction has a frequency range of ω_D which is the phonon frequency. The repulsion affects the electrons with energies on the scale of the Fermi energy. Averaging over the Fermi surface, one obtains

$$\langle\frac{4\pi e^2}{q^2 + k_s^2}\rangle = \frac{\alpha^2}{2} ln \frac{1+\alpha^2}{\alpha^2} \equiv \mu N(0) \tag{2.10}$$

where $\alpha^2 \equiv k_s^2/4k_F^2$. To put this on the same band width with the attraction one introduces a pseudo-potential

$$\mu^* = \frac{\mu}{1 + N(0)\mu ln(\varepsilon_F/\omega_D)} \tag{2.11}$$

With this approximation one reaches the BCS-Gorkov local effective interaction

$$-\frac{\tilde{\lambda}}{2}\int d^3x \tilde{\psi}_\sigma^+ \tilde{\psi}_{\sigma'}^+ \tilde{\psi}_{\sigma'} \tilde{\psi}_\sigma \tag{2.12}$$

where $\tilde{\psi}_\sigma \cong \Sigma' e^{i\boldsymbol{k}\cdot\boldsymbol{x}} c_{k\sigma}$. The prime means the sum over a shell of width ω_D. $\tilde{\lambda} = \lambda - \mu^*$ is the net effect of phonon induced attraction and coulomb repulsion (Note:$\tilde{\lambda}$ is the same V appearing in the review on the BdG equation).

2.1.2 BCS Theory

The key to understanding superconductivity is the attractive interaction between the electrons. The section above, rough but physically sound, should be treated more rigorously. In 1957, Bardeen, Cooper, and Schriffer (BCS)[14] published a microscopic theory based upon Cooper pair electrons bound by phonon interactions. The Cooper pair states, which are doubly occupied or empty quasiparticle states, show a lower energy with respect to the Fermi energy. So, in a superconductor, the Fermi sea is replaced with the condensate of Cooper pair states. The pairs greatly overlap with each other in space, and it is the strong pair-pair correlations in addition to correlations between the mates of a pair which are ultimately responsible for the rigidity of the superconducting wave function. The energy gap Δ, the energy required to create an excitation (or, it takes 2Δ break a pair) also comes from these correlations. At zero temperature, the condensate is complete and all the electrons take part in forming the superfluid. At finite temperatures, a small fraction of electrons evaporated from the condensate form a weakly-interacting gas of excitations which also extends through the whole system. [15] [16] [17]

The BCS Hamiltonian is

$$H = \sum_{k,\sigma} \epsilon_k c^*_{k\sigma} c_{k\sigma} + \sum_{k,k'} V_{k,k'} c^*_{k\uparrow} c^*_{-k\downarrow} c_{-k'\downarrow} c_{k'\uparrow} \tag{2.13}$$

where $c's$ are creation/anihilation operators, and $V_{k,k'}$ is the effective attractive potential. The ground state,

$$|G\rangle = \prod_k (u_k + v_k e^{i\phi} c^*_{k\uparrow} c^*_{-k\downarrow})|0\rangle \tag{2.14}$$

is a condensate which is a phase coherent superposition of Cooper pair states. $|0\rangle$ is

the vacuum state. The phase ϕ turns out to be the phase of the macroscopic wave function of the condensate. This macroscopic phase of a single superconductor is completely arbitrary when talking about a single piece of superconductor. (Note that the GL equation does not determine the absolute phase also). This phase becomes important when determining the coupling between weakly connected superconductors (i.e. Josephson effect).

2.2 NS System

What happens when a superconductor is in contact with a normal metal?

2.2.1 Modified States at the NS interface and Bogolubov-de Gennes Equation

The states close to the interface are modified as a consequence of the competition of the N and S orders. Before going into the transport phenomena, let's first look at some solutions from the famous Bogoliubov-de Gennes(BdG) equation for a ballistic situation. The BCS-Gorkov Hamiltonian is

$$H_{eff} = \int dr \sum_{\sigma} \psi_{\sigma}^{+}(r) H_0 \psi_{\sigma}(r) + \int dr \{ \frac{V(r)}{2} \sum_{\sigma,\sigma'} \psi_{\sigma}^{+}(r) \psi_{\sigma'}^{+}(r) \psi_{\sigma'}(r) \psi_{\sigma}(r) \} \quad (2.15)$$

Where $V(r)$ is the pseudo-potential $\tilde{\lambda}$ that appeared in the last section, H_0 is the single particle Hamiltonian, σ is the spin, and r is the position. The mean field

approximation for the spin singlet is

$$H_{eff} = E_0 + \int dr \sum_{\sigma} \psi_{\sigma}^{+}(r) H_0 \psi_{\sigma}(r) + \int dr \{\Delta \psi_{\uparrow}^{+}(r) \psi_{\downarrow}^{+} + \Delta^{*}(r) \psi_{\downarrow}(r) \psi_{\uparrow}(r)\} \quad (2.16)$$

where $E_0 = \int V(r)|f(r)|^2$. $f(r) =<< \psi_{\downarrow}(r)\psi_{\uparrow}(r) >>$ is the pairing amplitude and $<<>>$ stands for an average over all states. Then, $H = C + E_0 + H_{eff}$ (C stands for C number which arises from the interchange of the two field operators in the kinetic energy), where

$$H_{eff} = \int dr \begin{pmatrix} \psi_{\uparrow}^{+} & \psi_{\downarrow}(r) \end{pmatrix} H(r) \begin{pmatrix} \psi_{\uparrow}(r) \\ \psi_{\downarrow}^{+}(r) \end{pmatrix} \quad (2.17)$$

with

$$H(r) = \begin{pmatrix} H_0(r) & \Delta(r) \\ \Delta^{*}(r) & -H_0(r) \end{pmatrix} \quad (2.18)$$

This is the Bogoliubov-de Gennes Hamiltonian. The eigenvectors

$$\Psi_n(r) = \begin{pmatrix} u_n(r) \\ v_n(r) \end{pmatrix} \quad (2.19)$$

satisfy the Bogoliubov-de Gennes equation

$$H(r) \begin{pmatrix} u_n(r) \\ v_n(r) \end{pmatrix} = E_n \begin{pmatrix} u_n(r) \\ v_n(r) \end{pmatrix} \quad (2.20)$$

with eigen-energies $E_n^2 = \varepsilon_n^2 + \Delta(r)^2$. H_{eff} can be diagonalized by the transformation

$$\begin{pmatrix} \psi_{\uparrow}(r) \\ \psi_{\downarrow}^{+}(r) \end{pmatrix} = \sum_{n} \begin{pmatrix} u_n(r) & -v_n^{*}(r) \\ v_n(r) & u_n^{*}(r) \end{pmatrix} \begin{pmatrix} \gamma_{n\uparrow} \\ \gamma_{n\downarrow}^{+} \end{pmatrix} \quad (2.21)$$

and it yields

$$H_{eff} = E_G + \sum_{n>0.\sigma} E_n \gamma^+_{n\sigma} \gamma_{n\sigma} \tag{2.22}$$

where the ground state energy is

$$E_G = C + E_0 + \sum_{n>0} E_n = -2 \sum_{n>0} E_n \int dr |v_n(r)|^2 \tag{2.23}$$

The pairing amplitude is

$$f(r) = << \psi_\downarrow(r)\psi_\uparrow(r) >> = \sum_{n>0} u^*_n(r)v_n(r) - \sum_{n>0} u^*_n(r)v_n(r) << \gamma^+_{n\sigma}(r)\gamma_{n\sigma}(r) >> \tag{2.24}$$

For a ballistic SNS system (the size of the normal region is on the scale of the elastic mean free path l), the solution for the normal region includes four-fold degenerate solutions which can be written as [2] [3] [18]

$$\psi^\pm_e = \begin{pmatrix} 1 \\ 0 \end{pmatrix} \exp(\pm i q^+ r) \tag{2.25}$$

with $\hbar q^+ = \sqrt{2m}\sqrt{E_F + E}$. And,

$$\psi^\pm_h = \begin{pmatrix} 0 \\ 1 \end{pmatrix} \exp(\pm i q^- r) \tag{2.26}$$

with $\hbar q^- = \sqrt{2m}\sqrt{E_F - E}$. Here, the state is the total state and E is the total energy. In the superconductor, the solutions are electron-like and hole-like bogolons

$$\psi^\pm_e = \begin{pmatrix} u e^{i\phi} \\ v \end{pmatrix} \exp(\pm i k^+ r) \tag{2.27}$$

$$\psi_h^{\pm} = \begin{pmatrix} ve^{i\phi} \\ u \end{pmatrix} \exp(\pm ik^- r) \tag{2.28}$$

where $\hbar k^+ = \sqrt{2m}\sqrt{E_F + (E^2 - \Delta^2)^{1/2}}$ and $\hbar k^- = \sqrt{2m}\sqrt{E_F - (E^2 - \Delta^2)^{1/2}}$, and

$$u = \frac{1}{\sqrt{2}}[1 + (1 - \frac{\Delta^2}{E^2})^{1/2}]^{1/2} \tag{2.29}$$

$$v = \frac{1}{\sqrt{2}}[1 - (1 - \frac{\Delta^2}{E^2})^{1/2}]^{1/2} \tag{2.30}$$

2.2.2 Andreev Reflection

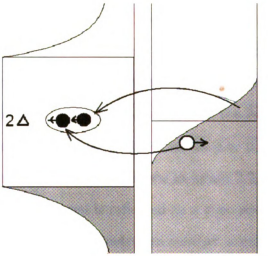

Figure 2.2: Schematic picture of Andreev reflection

The supercurrent inside the bulk superconductor is carried by Cooper pair states. When a normal current runs into a superconductor through a NS interface, part of the current has to transform into supercurrent, the rest will go through charge relaxation and then become supercurrent. If the energy of the electron in the normal metal is higher than the superconducting energy gap Δ, it will go into the superconductor and go through charge relaxation which can occur on the scale much longer than the superconducting phase coherence length. But, if the electron

energy is less than the energy gap, it can not go in because there are no available single particle states. Andreev [19] came up with a novel double-particle reflection process that solved the problem (shown in Figure 2.2) Andreev discovered that the solutions for the normal region of the Heisenberg equation of motion are of the form

$$\begin{pmatrix} u \\ v \end{pmatrix} = A \begin{pmatrix} 1 \\ 0 \end{pmatrix} e^{ik_1 x} + B \begin{pmatrix} 0 \\ 1 \end{pmatrix} e^{ik_2 x} \tag{2.31}$$

where $k_1 = \hat{n}w/v$ and $k_2 = -\hat{n}w/v$ are the wave-vectors for an electron and a hole respectively. $\hat{n}$ is the unit vector of momentum and $v = p_F/m$ (p_F is the Fermi momentum). The first term represents an incident particle(hole) and the second term represents a reflected hole(particle). Notice the k_1 and k_2 have completely opposite sign. For energy less than Δ, u and v decrease exponentially inside the superconductor. The solution certainly reminds us of the results from the BdG equations. The four-fold degenerate solutions describe the NS interface as a conjugate "mirror" where we find the "object" states (i.e. particles) and their "image" states (time reversed holes). As shown in figure 2.2, an incident electron with energy ε above the Fermi-level is reflected as a time-reversed hole and charge of 2e is transferred into the superconductor, in another words, adding a Cooper pair into the superconductor. Likewise, a hole can be reflected as an electron and 2e (or a Cooper pair) is removed from the superconductor. This actually should be noticed from the off-diagonal terms of the Hamiltonian in the BdG equation with Δ corresponding to creating a pair, and Δ^* corresponding to annihilating a pair. On the superconductor side

$$\begin{pmatrix} u \\ v \end{pmatrix} = \frac{c}{2} \begin{pmatrix} \sqrt{1 + vnk_s/\omega} \\ -i\sqrt{1 - vnk_s/\omega} \end{pmatrix} e^{ik_s r} \tag{2.32}$$

where $nk_s = v^{-1}\sqrt{\omega^2 - \Delta^2}$. The interesting aspect of the Andreev reflection is the

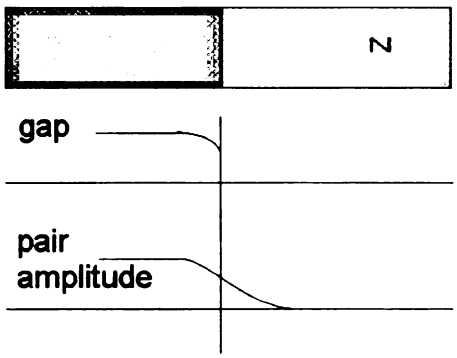

Figure 2.3: Schematic picture of the proximity effect

coherent interference of these modified states because particles and holes do obtain the superconducting phase through Andreev reflection. As will be discussed further in the next section, the phase coherence near the interface is critical for the proximity effect.

[For more exposure on both experimental details and theories regarding Andreev reflection can be found in this excellent paper by Blonder et al. [20]]

2.2.3 Proximity Effect

Proximity effect describes the presence of superconducting order inside the normal metal in a NS system, even though there is no attractive potential between the electrons. [7] [21] Obviously, this is just the continuation of the last section because proximity effect is originated from Andreev reflection. The pairing amplitude, as shown in figure 2.3, is nonzero in the normal side. The superconducting order parameter decays exponentially inside the normal metal over a characteristic length (thermal length) $L_T = \sqrt{\hbar D/2\pi kT}$.

For a NS system, the phase coherence length, an energy-dependent quantity, is

different for the ballistic case and the diffusive case. [22]

$$L_E = v_F t = \frac{\hbar v_F}{2E} \tag{2.33}$$

where $t = \hbar/2E$ is the time that the electron and hole wave-functions remain phase-coherent, and v_F is the Fermi velocity. For the diffusive case,

$$L_E = \sqrt{Dt} = \sqrt{\frac{\hbar D}{2E}} \tag{2.34}$$

In the diffusive limit, from both the Andreev's solutions and the BdG solutions, the conductance depends on the interference of the states in the normal region close to the interface and is proportional to

$$\sigma \sim k_F |\psi_e + \psi_h|^2 = k_F[|\psi_e|^2 + |\psi_h|^2 + 2Re(\psi_e \psi_h^*)] \tag{2.35}$$

which is an energy-dependent quantity. So, the Ginzberg-Landau order parameter $\psi(x)$ overlooks this energy-dependence on a scale less than L_E in which the interference of the states is energy-dependent. When $E \ll \Delta$, $Re[\psi_e \psi_h^*] \sim cos\varphi_{eh}$. For $E = 0$,

$$Re(\psi_e \psi_h^*) \sim cos\varphi_{eh} = 0 \tag{2.36}$$

For $E > 0$,

$$k_e - k_h = \sqrt{k_F^2 + 2mE/\hbar^2} - \sqrt{k_F^2 - 2mE/\hbar^2} = 2E/\hbar^2 v_F \tag{2.37}$$

φ_{eh} builds up as we go away from the interface. The interference is lost on a scale of $L_E = \hbar^2 v_F/2E$ for ballistic systems or $L_E = \sqrt{\hbar D/2E}$ for diffusive systems. Note that the energy E is the total particle energy which includes the thermal energy. The superconducting order can extend through out the normal region if the sample

length L is less than the phase coherence length L_ϕ. When $L > L_\phi$, the phase coherent inference is cut off by L_ϕ. Superconductivity can be thought of as a sort of rigidity. And, this rigidity can be maintained even in the normal region by phase coherent Cooper pair states.

2.3 SNS Josephson Effect and Andreev Bound States

The Josepshon effect [23] [24] describes how a superconductor with long-range order couples with another superconductor through a weak link. The coupling can be expressed in the form of

$$I_S = I_C sin\phi \tag{2.38}$$

where I_C is the critical current (maximum supercurrent can pass through the device), ϕ is the phase difference between the two superconductors, and I_S is the supercurrent.

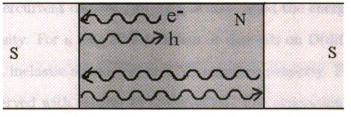

Figure 2.4: Schematic picture of the Andreev bound states formed in a SNS long junction with $L < L_\phi$

The microscopic picture of the Josephson effect is the Andreev bound states formed between the two NS interfaces. [2] As shown in figure 2.4, an electron reflected as a hole at the left interface gets to the other NS interface without losing phase, and gets reflected again, thus, forms an Andreev bound state. This is an

energy-dependent process because $L_E = \sqrt{\hbar D/2E}$. [25] For the states with large E, phase coherence is hard to be maintained. While, for the low energy states, the phase coherence is maintained because L_E is long enough. The Thouless energy $E_{Th} = \hbar D/L^2$, which is the energy broadening as a particle goes across the sample, is a consequence of the system coupled with the environment. It turns out that, as Δ governs the energy scale for ballistic SNS transport, E_{Th} [26] sets the energy scale for long diffusive junctions.

The supercurrent inside the normal region can be derived from the quasiclassical theory(reviewed in chapter 7) and has the form

$$I_S = (\sigma_N/2) \int d\varepsilon Im[j(\varepsilon)] f_0(\varepsilon) \tag{2.39}$$

in which the integrand is a product of Spectral supercurrent density $Im[j(E)]$ and an asymmetric distribution function f_0.

2.4 Spectral Supercurrent Density

Spectral supercurrent density $Im[j(E)]$ is also called the energy spectrum of supercurrent density. For a long SNS junction, it depends on D(diffusion constant), sample geometry, inelastic scattering, and NS interface property. For a SNS device, $Im[j(E)]$ is conserved with respect to the position. The expression of $Im[j(E)]$ for the diffusive situation is given in chapter 7 and the AppendixC. Let us first look at the ballistic case.

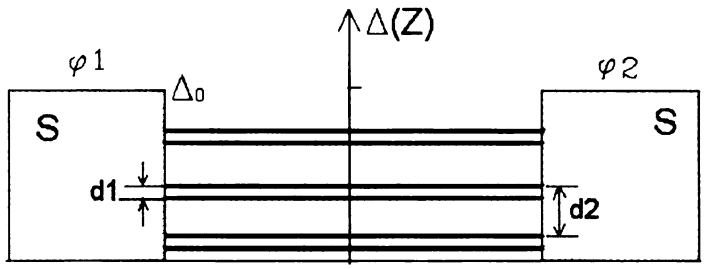

Figure 2.5: Energy levels of the excitations in the normal region at a fixed value of electron velocity [2]

2.4.1 Ballistic case

Exact solutions [2] can be obtained by solving the BdG equation for a Ballistic SNS junction. The eigenenergies are

$$E_n^{\pm} = \frac{\hbar v_F}{2L^*}[2(n\pi + \varphi(E)) \mp \phi] \tag{2.40}$$

where $\varphi(E) = arccos(E/\Delta)$ is a slow varying function of energy. At low energies $E \ll \Delta$, we have $\varphi(E) \approx \pi/2$. So we have

$$E_n^{\pm} = \frac{\hbar v_F}{2L^*}[2\pi(n + 1/2) \mp \phi] \tag{2.41}$$

which depends only on ϕ (the phase difference between the superconductors). The effective sample length (with proximity correction) is $L^* = L + \hbar v_F/\Delta_0$. $E_n^{\pm}$ corresponds to the energy states going to right and left. When phase difference is zero, energy states going both directions coincide and the total supercurrent is zero. When the phase difference is not zero, the energy spectra for the counter-flowing supercurrents are separated so that net current density appears. As is shown in figure 2.5, due to the phase difference ϕ, the energy separation between two adjacent levels going into the same direction is $d2 \approx \pi v_F/L^*$, and the separation between the levels going opposite directions is $d1 = d2 \times (\phi/\pi)$ which depends on ϕ. A graph of

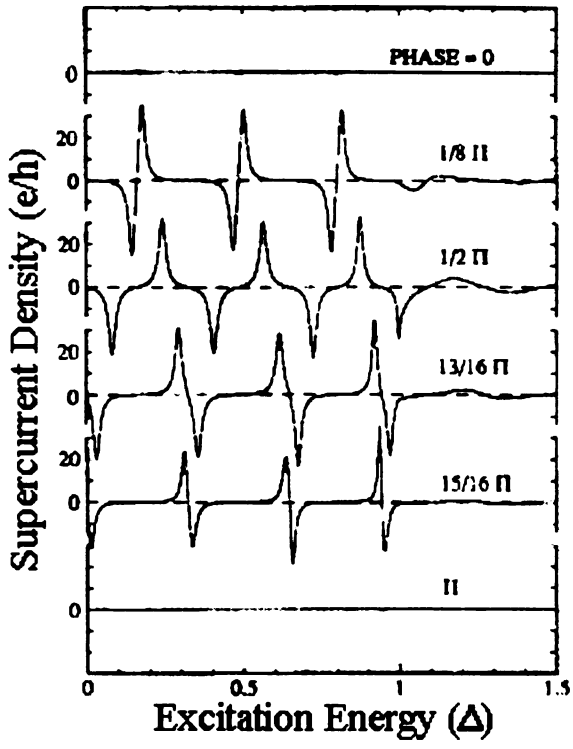

Figure 2.6: Spectral supercurrent density vs. excitation energy for different phase differences for a 3-terminal superconductor-semiconductor-superconductor device [3]

$Im[j(E)]$ for a three-terminal superconductor-semiconductor-superconductor device is plotted versus energy in Figure 2.6, in which each curve corresponds to a fixed phase difference [3].

2.4.2 Diffusive case

For long SNS junctions, things are complicated by the diffusion process and the broadening of the energy band. One has to solve for the Green's functions of the quasiclassical equations to obtain $Im[j(E)]$. A result from my calculations by the quasiclassical approach is shown in Figure 2.7. Compared with the ballistic case, there are two dramatic differences. (1) The δ function for the peaks are widened by the factor of E_{Th} which is about 5μV. (2) The amplitude of $Im[j(E)]$ is reduced at higher energies because of the energy dependence of the correlation length $L_E = \sqrt{\hbar D/2E}$. For higher energies, fewer Cooper pairs can survive the trip from

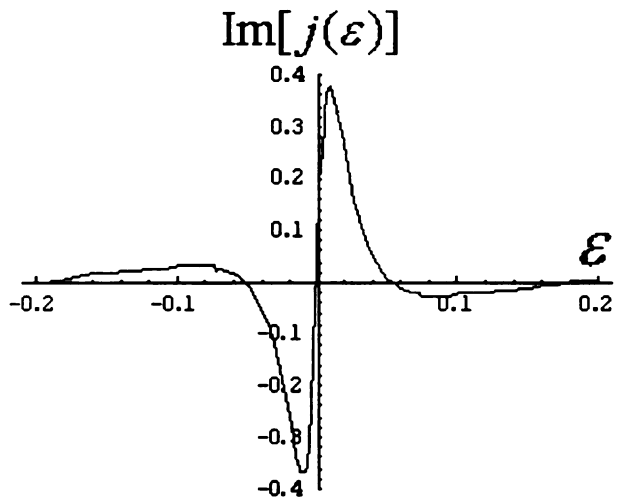

Figure 2.7: Calculated spectral supercurrent density by quasiclassical approach. The units for energy is meV

one NS interface to the other.

2.5 Distribution Functions

The distribution function describes how the occupation of the states is affected by temperature and applied potential. It turns out the distribution function depends on the sample length compared with electron-phonon length L_{e-ph} and electron-electron length L_{e-e}. In figure 2.8, distribution functions are shown for the N-n-N device at zero temperature. When $L > L_{e-ph}$, the electrons completely thermalize because the electron phonon interaction carries away all the heat generated inside the normal wire. When $L_{e-e} < L < L_{e-ph}$, electrons exchange energies with each other so that the effective temperature can reach much higher than the lattice temperature. Local heating is produced because there is not sufficient electron-phonon interaction to carry out the heat. This is called the hot electron regime. When $L < L_{e-e}, L_{e-ph}$, the single electron energy is conserved. The

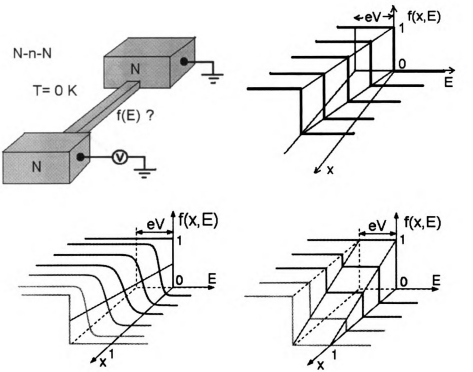

Figure 2.8: Distribution functions for different sample lengths for N-n-N structures. Upper right: $L > L_{e-ph}$; lower left: $L_{e-e} < L < L_{e-ph}$; lower right: $L < L_{e-e}, L_{e-ph}$ [4]

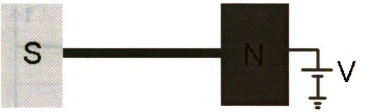

Figure 2.9: A S-n-N system with N elevated by voltage V

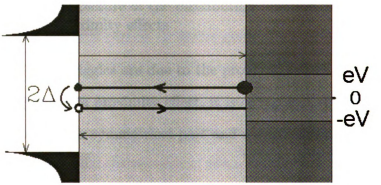

Figure 2.10: A schematic picture of how a quasiparticle distribution function varies in space. The solid dot stand for an particle and the circle stands for an Andreev reflected hole. The size of the circles stand for the amplitude of distribution function of the particle/hole

Boltzmann equation with zero inelastic collision ($\partial_x^2 f = 0$) gives a distribution of staircase [4]. This is the regime in which our experiment is performed.

The distribution function for the SN system shown in Figure 2.9 is quite different than the N-n-N. A schematic picture showing how the distribution function changes inside the normal wire is shown in figure 2.10. First of all, the Andreev reflection is a two-particle process. So, the excitation ranges from -eV to eV. The second is that the distribution function still varies linearly, but over the distance of $2L$ instead of L. For a particle at the normal reservoir going to the left, its distribution function reaches $1/2$ at the right NS interface. This can be obtained through the relationships $f(E) = f(-E)$(two particle process) and $1 - f_h(-E) = f(E)$(boundary condition). Figure 2.11 shows schematically a real distribution (including the correction of proximity effect) at a point very close to the

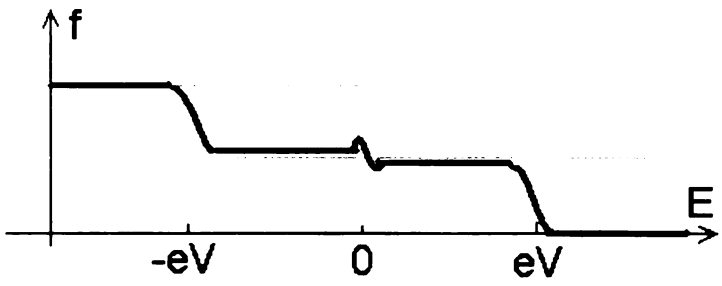

Figure 2.11: A schematic picture of the distribution function with correction due to both temperature and proximity effects

NS interface. The small wiggles are due to the proximity effect.

For the nonequilibrium proximity effect, it is convenient to resolve the distribution function into a symmetrical part and a symmetrical part

$$2f(E) = 1 - (f_0 + f_1) \tag{2.42}$$

where f_0 is the antisymmetric part which corresponds to the effective temperature change in the system, and the f_1 is the symmetric part which corresponds to the effective chemical potential shift or charge imbalance. This is why f_0 and f_1 have different x-dependence inside the wire. For a SNS system, f_0 and f_1, which are the driven forces for heat current and the charge current, are coupled through supercurrent density $Im[j(E)]$.

2.6 π Junction

π junction refers to a π phase shift to the phase difference ϕ in the Josephson relation so that it changes from $I_S = I_C \sin\phi$ to $I_S = I_C \sin(\pi + \phi)$. As discussed above, inside a long Josephson junction ($l \ll L < L_\phi$), there are supercurrent

carrying states flowing into both directions and the net current

$$I_S = (\sigma_N/2) \int d\varepsilon Im[j(\varepsilon)] f_0(\varepsilon) \tag{2.43}$$

is the result sum of all supercurrent-carrying states. When the phase difference ϕ is zero, the supercurrent flowing in both directions cancels each other [3] and $Im[j(\varepsilon)] = 0$. When a finite $\phi \neq 0$ is produced (by either applying magnetic flux or driving current), the currents carried by states going into opposite directions no longer cancel each other. The direction of the net supercurrent depends on which direction most current carrying states are going. In addition to the phase difference ϕ which determines each supercurrent-carrying state, the antisymmetric distribution function f_0(occupation of the states) selects which states to exist. As a normal injection increases, the energies of the quasiparticles change also, so, the occupation of the states changes. By shifting the occupations of the quasiparticle states along the energy spectrum, the direction of the net supercurrent is alternated. So, when we increase the injected quasiparticle current from zero, the supercurrent decreases until the net supercurrent changes direction when it reaches a certain energy. This is when π junction occurs. It appears in the Josephson relation as a π phase shift to the phase difference ϕ.

The appearance of the π junction can take place by controlling the width of the staircase distribution function f_0. For our experiment in which we inject quasiparticle current, the width of f_0 is $2eV$ (from $-eV$ to eV). (figure 2.12) The spectral supercurrrent density is an odd function of energy and is not affected by either normal injection or the temperature. Then, the sign of the integrand of the net supercurrent 2.43 depends on the value of eV. For $eV_N < E_0$, the junction is at zero phase state(the sign of the product of f_0 and $Im[j(E)]$ is positive); for $eV_N \sim E_0$, I_C goes to zero; and for $eV_N > E_0$, π phase state appears (the sign of the

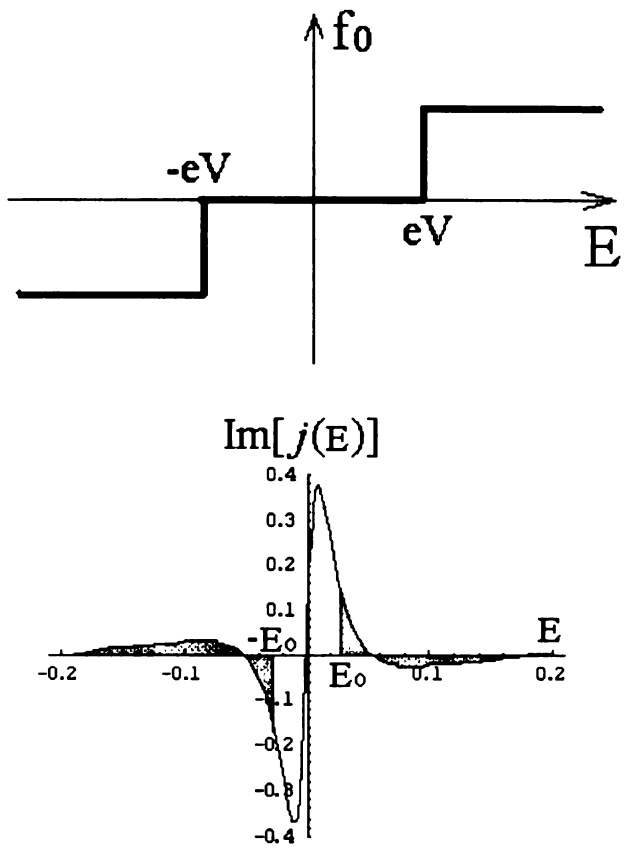

Figure 2.12: Antisymmetric distribution function f_0 (upper graph) and the spectral supercurrent density

product of f_0 and $Im[j(E)]$ is negative).

2.7 Summary

As discussed in earlier sections, the BdG formalism can strictly solve the NS problem for the ballistic case, but is difficult to solve for the diffusive case in which the length greatly exceeds the elastic mean free path l. The Quasi-classical theory, a application of the Gorkov equations to the dirty limit, has become a powerful tool for many practical diffusive calculations. I will discuss quasiclassical theory in chapter 7. There is also the matrix approach which is based on Landauer's formula.

More details on discussing the differences is provided in the paper by Ralph and Ambegaokar. [27]

Chapter 3: Fabrication Methods

Introduction: Micro-fabrication has become the key technology that enables the dynamic growth of the IC industry and fundamental research of small systems. The fabrication techniques include

- Photolithography
- Electron beam lithography
- X-ray lithography
- soft-lithography
- deep UV resist technology
- polymer and organic methods

It seems like organic methods will be the future of nano-fabrication since they pull together physics, chemistry, electrical engineering, chemical engineering, biology, and even medical sciences. The fabrication methods involved in this thesis are surface preparation, photolithography, electron beam lithography, and etching.

3.0.1 Surface Preparation

Contaminants cause serious problems with lithography processes so they must be removed properly before resist coating. Typical contaminants are:

- Dust from dicing the wafer
- Atmospheric dust
- Resist and developer residue from previous lithography
- Bacteria

- Solvent residue from previous chemical processes
- H_2O residue
- Oil

A nitrogen gun can remove dust that falls upon the surface of the substrate, laser scribing can remove the dust from dicing the wafer, Micro (a detergent) can remove the oil particles, plasma etching can remove resist residue, and deionized (DI) water can remove most of the bacteria.

After removing these contaminants, start the fine cleaning process by first putting the substrate into acetone and put in the ultrasonic bath for 5 to 10 minutes. Often it helps to preheat the acetone. But, the temperature should not exceed 68^0C which is the flash point of acetone. Then, rinse the substrate with Isopropyl alchohol(IPA). Last, rinse again with DI water. Finally, blow dry it with nitrogen gun.

3.1 Photolithograhy

3.1.1 Photo Resist Coating

Thin film spin coating is often the first step of the whole fabrication. It is a process to coat the substrate with layer(s) of resist (such as photo resist or e-beam resist) by using a spinner with controllable spin speed. It normally includes the following steps:

- Mount substrate on the stage

  The substrate should be placed in the center of the stage so that the film will be uniform. Then, apply vacuum to hold the substrate down.

- Use Nitrogen gun to clean the surface of the substrate.

This is to blow away any dirt that may fall onto the surface while transferring. Use gentle blow if there are already some features on the substrate to avoid damage.

- Use pipette to apply liquid resist onto the center of the substrate
  The resist will form a ball at the center. Squeeze the pipette uniformly to avoid bubbles because they can cause singularities on the film.

- Immediately start spinning by pressing the starting button.
  Centrifugal force will cause the drop of resist to move in waves away from the center of the substrate until a film of the resist is formed. The normal spin time is 1 minute.

- Wait
  Before removing the substrate, wait for 15 seconds to allow good adhesion between the resist and the substrate surface.

- Remove the substrate and put it into the baking oven.

One ought to practise in order to control the thickness and uniformity of the film. The thickness is normally determined by the concentration of the resist and spin speed. The thickness vs. spin speed curves for various resists with different concentrations are provided in the clean room. These numbers are generally good for wafer substrates. But, when the size of the substrate is very small, the film becomes thicker because the centrifugal force is reduced compared with the surface tension at the edge. For example, when spinning 4% PMMA onto a 7mm x 7mm Silicon substrate and onto a 5mm x 5mm substrate, the thicknesses of the films are 240nm and 400nm, respectively.

Though the range of the speed can be chosen from 1000 rpm to 6000 rpm, 2500 rpm is generally the minimum speed to ensure the uniformity of the film. The

thickness and the concentration of the resist film should be chosen to optimize the lithography processes. For example, if one wants to fabricate very fine features on the substrate, the aspect ratio can not be too large. This means the resist can not be too thick. Meanwhile, the resist can not be too thin because it can cause problems with the lift-off. Normally, the resist should be 3 times the height of the features.

3.1.2 Photo Resist Baking

The baking time is minimum 45 minutes. Extending the baking time helps to improve the uniformity of the resist. This is only necessary when very fine features are desired. The baking temperature is usually 95^0C. This temperature is not fixed under certain circumstances. For example, if there are already some features (i.e. nano wires) underneath the resist, baking at 95^0C may cause nucleation and damage the wires. One has to lower the temperature to avoid damage.

3.1.3 Exposure

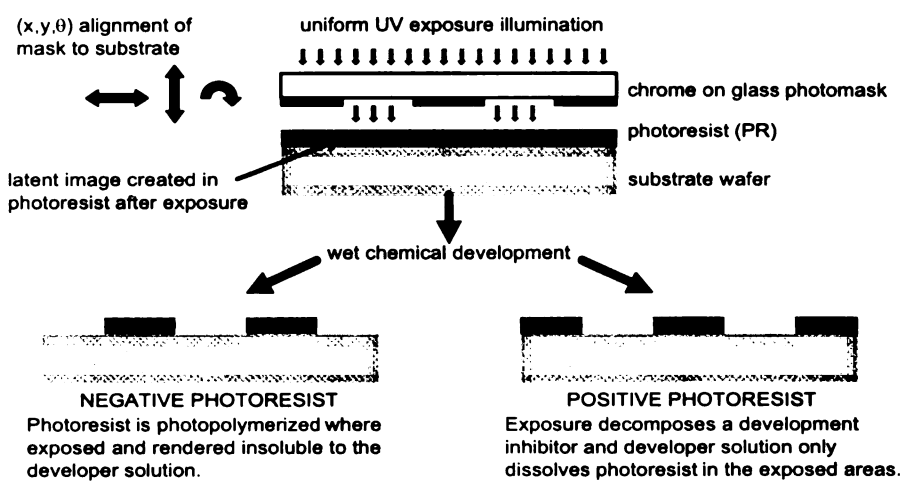

Figure 3.1: A schematic picture of photo printing

Exposing the photo resist(contact printing shown in figure 3.1) is done by using UV light (wavelength 345 nm) shining through the mask which is in contact with the

resist. Because the exposure is through the mask, the volume of the resist exposed depends on the interference and diffraction of the UV light, as well as the thickness and density of the resist. The proximity effect, which describe the widening effect of the features due to the interference of the UV light, becomes critical, especially when the feature size is very small. The proximity effect can be reduced by decreasing the thickness of the photo resist. But, the resist can not be too thin because it might be difficult to produce a clear undercut and cause trouble for the liftoff. Generally, it is harder to have good undercut when the resist is too thin.

3.1.4 Development

Right after the exposure is the resist development. Holding a corner of the substrate with your tweezer, submerge into photo-developer 452. Slowly shake it in the liquid back and forth for 45 seconds. Then, take it out quickly and submerge into DI water for 30 seconds. Then, blow dry with the nitrogen gun. Be careful that you do not point too close to the substrate if you already have some features on it. The pressure of nitrogen may damage them.

3.1.5 Evaporation and Liftoff

The metal evaporation is done in a Edward Auto306 thermal evaporator which has a base pressure 2×10^{-7} torr. The current and evaporation rate for some common metals are listed in table 3.1. The liftoff is a process to remove the excessive metal and resist on the substrate. This is normally done in hot acetone (heated to 68^0C). Observe closely and take the substrate out as soon as the liftoff is complete. Rinse with Acetone, IPA, and DI water.

metal	current(Amp)	evaporation rate$\AA$/s
Ag	2.2	3
Al	2.6	2.8
Au	2.4	3.2

Table 3.1: Metal deposition current and rate for Edward Auto306 thermal evaporator

3.1.6 Photo-alignment

Photo-alignment is to optically align the substrate with the mask so that the exposure takes place at the desired areas on the substrate. This is necessary when putting together different metal patterns. The goal of alignment is to overlay some alignment marks on the substrate with the alignment marks on the mask. Obviously, the marks put down on the substrate have to be exactly the same as those on the mask. This has to be emphasized because some choose to put down alignment marks by e-beam writing. The magnification can be off a little bit so that the marks may be slightly different than those on the mask. This will reduce the alignment accuracy. The best method is to have two masks with identical alignment patterns on them. This way, one can put down the alignment marks on the substrate by optical lithography. Another factor that affects the alignment accuracy is the magnification of the lens. 200X magnification or better is needed when 0.1 micron accuracy is desired. The third factor that affects the alignment accuracy is the thickness of the resist. The resist is in contact with the mask. So, the distance between the marks on the mask and the marks on the substrate is at least the thickness of the resist. When it is too thick, it is impossible to have both sets of marks in focus simultaneously.

3.2 Electron Beam Lithography (EBL)

Electron beam lithography (EBL) is a specialized technique for creating the very fine patterns through scanning a beam of electrons across a substrate covered

with a e-beam resist film which is sensitive to the electrons. Similarly to the photo development, the exposed resist is removed through e-beam development. Figure 3.2 is a schematic picture of a typical e-beam process. The process of forming the beam of electrons and scanning it across a surface is very similar to what happens inside a television, but EBL typically has three orders of magnitude better resolution.

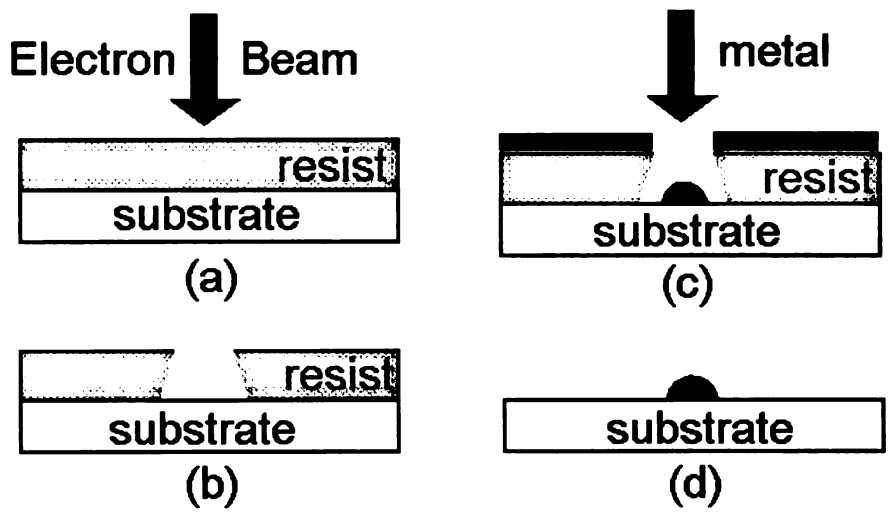

Figure 3.2: E-beam Process: (a) Spin-coat the substrate with e-beam resist. Expose the resist with electron beam. (b) Develop the resist. (c) Metal deposition. (d) After lift-off

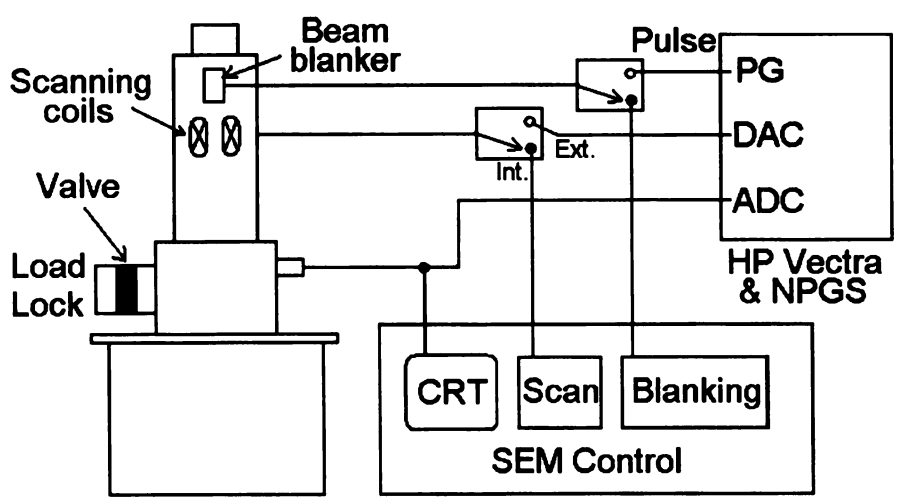

Figure 3.3: Block diagram showing the major components of a typical electron beam lithography system

The main attributes of the EBL are

- very high resolution, almost to the atomic level
- flexible technique that can work with a variety of materials and an almost infinite number of patterns
- slow, being one or more orders of magnitude slower than optical lithography
- expensive and complicated - electron beam lithography tools can cost many millions of dollars and require frequent service to stay properly maintained

The scanning electron microscope (SEM) JEOL 840 (see figure 3.3 is used for imaging samples. It is also equipped with a computer-controlled pattern generating system enabling the writing of patterns for devices with feature sizes as small as 50 nm. Some of the features on the SEM/EBL system include:

- Acceleration voltage: up to 40 kV
- Filament type: Tungsten
- Beam size: 8 nm at 35 kV
- Pattern design: DesignCad
- Pattern formation: Vector scan
- Pattern generating: Nabity Lithography system
- Beam blanker: 8 MHz electromagnetic

3.2.1 Electron-Solid Interaction and Proximity Effect

[The following is a brief description of how the electron solid interact when electrons going into the substrate. For more exposure, refer to the book on microlithography by Mark A. McCord and Michael J. Rooks [5].]

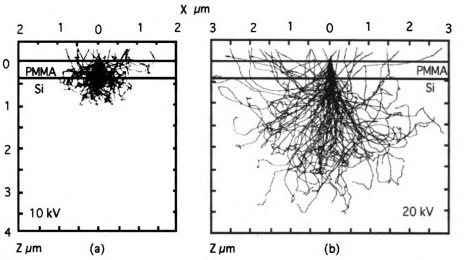

Figure 3.4: Simulated profile of the energy absorbed from an electron beam exposure [5]

As the electrons penetrate the resist, they experience many small angle scattering events (forward scattering), which tend to broaden the initial beam diameter. As the electrons penetrate through the resist into the substrate, they occasionally undergo large angle scattering events (backscattering) which are responsible for causing the proximity effect. During this process the electrons are continuously slowing down, producing a cascade of low voltage electrons called secondary electrons. Figure 3.4 is a simulated picture of the traces of the scattering of the incident electrons.

Forward Scattering

As the electrons penetrate the resist, some fraction of them will undergo small angle scattering events, which can result in a significantly broader beam profile at the bottom of the resist (see figure 3.4). The increase in effective beam diameter in nanometers due to forward scattering is given empirically by the formula $d_f = 0.9(Rt/V_b)^{1.5}$ [5], where R_t is the resist thickness in nanometers and V_b is the beam voltage in kilovolts. Forward scattering is minimized by using the thinnest possible resist and the highest available accelerating voltage.

Backscattering

For those electrons experiencing large angle scattering, they can return back through the resist at a significant distance from the incident beam, causing additional resist exposure. This is called the electron beam proximity effect. The range of the electrons depends on both the energy of the primary electrons and the type of substrate. The fraction of electrons that are backscattered, is roughly independent of beam energy, although it does depend on the substrate material. Normally, backscattering decreases with lower atomic number material.

Secondary Electrons

As the primary electrons slow down, much of their energy is dissipated in the form of secondary electrons with energies from 2 to 50 eV. They are responsible for the bulk resist exposure. Since their range in resist is only a few nanometers, they contribute little to the proximity effect. Instead, the net result can be considered to be an effective widening of the beam diameter by roughly 10 nm. A small fraction of secondary electrons may have significant energies, on the order of 1 keV. These so-called fast secondaries can contribute to the proximity effect in the range of a few tenths of a micron.

Proximity Effect Avoidance

To optimize the dose is always the first thing to do. Also, using bilayer resist with different e-beam sensitivity can reduce the forward scattering effect. Higher beam voltages, from 50 kV to 100 kV or more, also minimize forward scattering, although in some cases this can increase the backscattering. This method is extremely good if the substrate is very thin so that most of the electrons go right through. Meanwhile, by going to very low beam energies, where the electron range is smaller than the minimum feature size, the proximity effect can be eliminated.

The penalty is that the thickness of a single layer resist must also be less than the minimum feature size so that the electrons can expose the entire film thickness. It also makes is hard to focus. So, it is a limited method.

Proximity Effect Versus Dose of Exposure

I have done a series of tests to show how the dose affects the proximity effect (see SEM pictures in figure 3.5), and the relationship, shown in figure 3.6, is obtained.

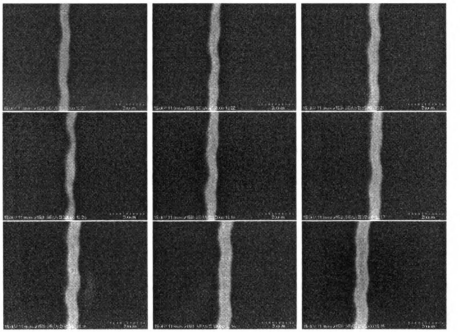

Figure 3.5: SEM pictures of a series of single paths (Ag lines) with following doses in nC/cm: 2.0, 2.1, 2.2, 2.3, 2.4, 2.5, 2.6, 2.7, and 2.8.

3.2.2 Electron Beam Writing

The pattern design is done by using DC6 designCAD and stored as designCAD file. A run file "filename.mef" is produced by the "mrf" command. This is the file that has all the writing conditions for each element of the pattern. Before writing, get the microscope in focus by focusing on a subject on the substrate. Try focusing

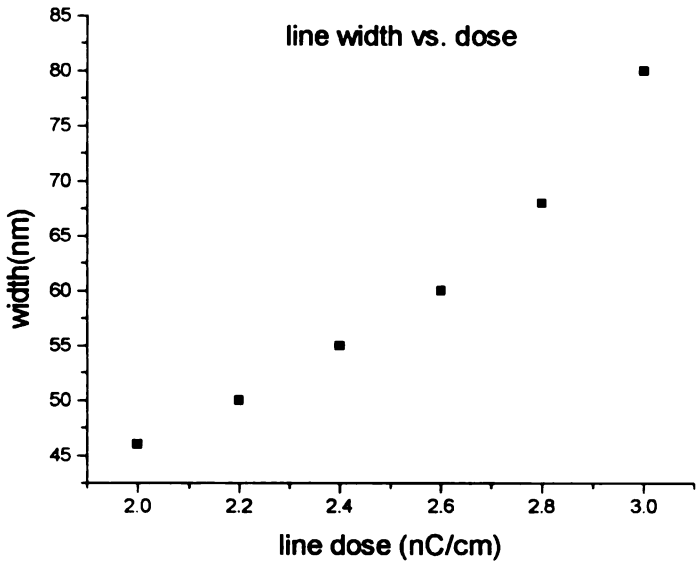

Figure 3.6: Width of the single path versus dose

in well at 200KX or better. Then, turn on the external mode, start the writing by a command "pg filename". The details are provided in the Nabity Menu book [28].

3.2.3 Development

Right after the writing is the resist development. Submerge the substrate into e-beam-developer MIBK(1:3). Slowly shake it back and forth for 55 seconds. Then, take it out quickly and submerge into IPA for 40 seconds. Then, rinse it in DI water and blow dry with a nitrogen gun. Be careful that you do not point too close to the substrate if you already have some features on it. The pressure of nitrogen may damage them. Evaporation and liftoff are identical to the photolithography.

3.2.4 Electron Beam Alignment

When multi-level Lithography process is needed, e-beam alignment becomes critical because the small features demand very high alignment accuracy. The first

step is to create an alignment file which includes the alignment marks inside some scanning windows. The alignment run file will control the beam to scan the windows and find the marks. Then, overlay the marks with the marks of the file. An offset will be computed when the overlay is done. This offset will be the offset when writing the pattern.

Take $0.1\mu m$ alignment accuracy for example, the smallest alignment window is around $4\mu mx4\mu m$. So, a 3-level alignment process is adopted. (table 3.2

	size of the marks	size of the windows	magnification
Level1	1mm	1mmx1mm	20X
Level2	30μmx30μm	40μm x 40μm	100X
Level3	3μmx3μm	4μm x 4μm	1000X

Table 3.2: 3-level alignment

The successful alignment has to be done by using both mechanical alignment (by moving the stage) and computational alignment (computer calculated matrix to shift the beam). The first is used at low magnification and the adjustment is rough. The purpose for the mechanical alignment is to set the sample as close to the center of the screen as possible. If you do not, the 3rd level alignment will be out of the range of the screen. The computational alignment is used for 2nd and 3rd level alignments (1st level too if you choose). Each time you do alignment the program deals with both translation and rotation by computing the matrix that adjusts the beam.

- Alignment at 20X:

  Overlay the alignment pattern from your alignment file with alignment marks as well as possible by moving the stage. On the JEOL monitor you can roughly see where you are. But, for more accurate position you have to trust only the computer monitor screen. You can check how close you are by going into the 2nd alignment level. If you see, at the first scan, that the marks are pretty much inside the windows (say 75%) you are ok. But, if you only see a

little bit of each mark appearing in the scanning windows, you will probably be in trouble when going into the 3rd level because the center of the sample may well be out of the range of the screen. Then, you have to go back to 20X, adjust the sample mechanically while scanning until the both sets marks overlay. At this moment it is ready to go into the 2nd level.

- 100X level:

  Try to overlay the pattern and the marks by moving each individual mark onto the real mark, then hit "r" (return) key. Repeat this process until you get exact overlay. Now, you are ready to go into 3rd level

- 1000X level:

  Note that there is still another factor that needs to be taken into consideration: shift of the center of beam with changing magnification from 100X to 1000X. This factor becomes important when going into high magnification. You have to measure the offsets and put them into the offset settings in your alignment file. The typical offset from 100X to 1000X is (4.6μm and 8.1μm). The alignment process is the same as that at 100X. Right after it is done, write pattern immediately with the command

  Pg filename a

  "a" calls for the computed matrix offset. It is important to remember to input the offset to your writing file also.

3.3 Actual Sample Making

3.3.1 Review of Methods

Fabrication Methods

I have tried several different fabrication methods to fabricate the sample. One of the reasons is that we did not initially have ion-milling in the evaporation chamber.

- The first method

  A gold pattern was first put down to serve as the alignment marks. Then an insulating layer of SiO (70 nm) was deposited on top of gold. Then, the normal wire and normal reservoir were put down by e-beam lithography with e-beam alignment. The last step was to put down the superconductor (Al) using the same alignment marks. The problem was the visibility of the Au pattern. SiO is an insulator, it is very hard to see through it. That made the alignment a pain. We could not go any thinner because the SiO has a minimum thickness about 70nm to maintain its insulating behavoir.

- Angle Evaporation

  The second idea was based on the angle evaporation method. The whole pattern is one e-beam pattern (figure 3.7). On the pattern, the reservoirs and the wire are separated. The idea is to bring the wire and the reservoirs in contact by evaporating at different angles. It requires an angle tilting during the evaporation. Though we designed the pattern and developed the skills for e-beam lithography, we did not pursue this idea because the tilting sample holder was not ready at the time.

I then tried two other methods both of which worked. They are described in detail in the later sections.

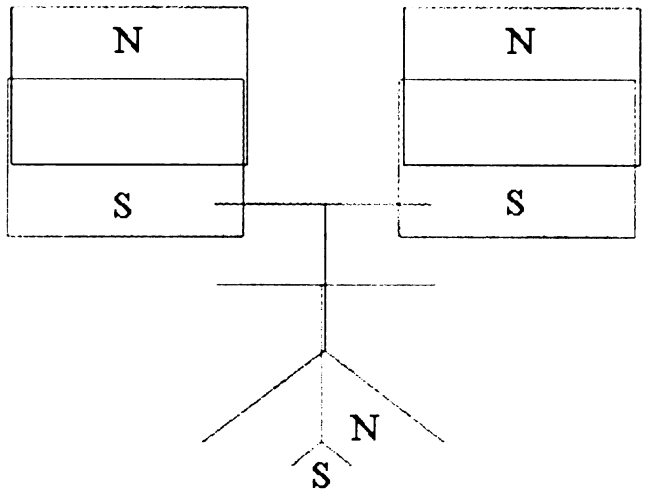

Figure 3.7: Schematics of an angle evaporation method. The two sets of patterns are from evaporations at different angles

Material Combinations

Meanwhile, I also tried different metal combinations for the normal conductor and superconductor. Below is a list of combinations I have tried.

- Pb-In-Au(90%,8%, and 2%) and silver

  Choosing Pb-In-Au was due to the fact that the surface oxidation of Pb-In-Au is very little. The problem is that when the film of Pb-In-Au is less than 100nm thick, pin-holes were formed.

- silver(Ag) and aluminum (Al)

  This works fine except that silver is not as stable as we desired. Ion-milling has to be applied to the first metal before the second metal is deposited.

- gold(Au) and aluminum (Al)

  I spent a lot of time on this because one of the first tests on a $0.5\mu m$ wide and $2\mu m$ long Au wire in contact with Al reservoirs had a resistance of 8 ohms. But, when I fabricated narrow wires the interface became insulating. This turns out to be the well known purple plague. There are alloys formed

between gold and aluminum and these alloys are insulators.

- Nb and Au

  I had problems with heating the substrate while sputtering Nb due to the small size of the substrate. The Nb film does not stick to the substrate very well. It becomes problematic during liftoff.

So, after all these tests, we chose Ag and Al.

3.3.2 Method 1: E-beam First, Photolithography Second

Unlike the traditional way of making samples (lay down the big features first by photo processes, then e-beam process to put down the nano wires), I first write the nano features and alignment marks with e-beam lithography. Then, with photo-alignment, I put down the normal reservoir and superconducting reservoirs as illustrated in figure 3.8. This method shortened the whole process almost by half. And, it avoids ion-milling the Al which can be rather difficult due to the tough oxide.

Substrate preparation

The commercial wafer is very clean already. I first spin-coat the surface with photo resist S1813. Then, bake it at 95^0C for 40 minutes. This is to protect the surface when it is diced into 7mm x 7mm square pieces. The surface is protected by the resist until it is washed away with acetone and IPA before spin coating the e-beam resist.

E-beam Process

- Resist Preparation

  The e-beam resist is a bilayer resist in order to obtain good undercut. The

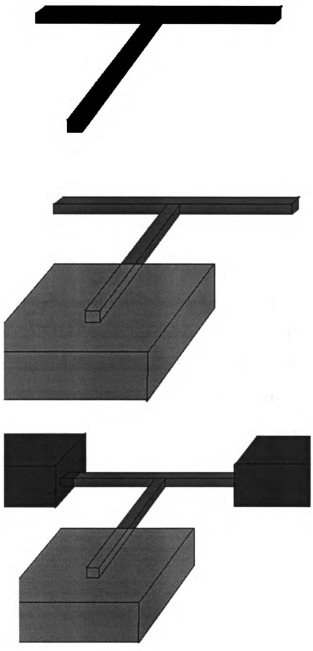

Figure 3.8: Three Steps of making the the sample

Bilayer Resist	Spin	Thickness	Bake
P(MMA/MAA)6%	5750 rpm (1 min.)	260nm	160^0C, 1 hour
PMMA 4%	5950 rmp (1 min)	140 nm	160^0C, 2 hours

Table 3.3: Spin and baking conditions for $7mm \times 7mm$ Si substrate

magnification	measured beam current	dose	step size
1000X	7 pC	2.8 pC/cm	13.7 Å

Table 3.4: E-beam writing conditions for single path

develop	rinse
MIBK 1:3 for 55 seconds	DI water for 30 seconds

Table 3.5: E-beam resist Development

bottom layer is co-polymer (P(MMA/MAA)6%) The top is PMMA. The total thickness of the bilayer resist is around 400nm. Two small drops of silver paint are put on top of the resist symmetrically for e-beam focusing.

- E-beam writing

  Instead of using mask as in photolithography, pattern is designed with CAD and saved as a CAD file. A run file can be made by using software DC6 so that all the writing conditions for each part of the pattern are defined. These conditions include layer, color, dose, offset, beam current, step size, line spacing, magnifications, pause, etc. Then, the "pg filename" command starts the writing. For a single path feature, the writing and development conditions are shown in Tables 3.4 and 3.5.

- Thermal evaporation of Ag

- Liftoff

  The liftoff is done in heated acetone (58^0C) for 1 minute. Often it takes much longer when the undercut is not good or the feature is very small.

Metal	current	deposition Rate	thickness
Silver (99.999%)	2.3 Amp	3.2 Å/S	65 nm

Table 3.6: Thermal evaporation of the nanowire

resist	spin	thickness	bake	expose	develop
S1805	4500 rpm	5000$\AA$	70^{0}C	3.4 seconds	45 seconds

Table 3.7: photo printing condition

Metal	current	deposition Rate	thickness
Silver (99.999%)	2.3 Amp	3.2 $\AA$/S	220 nm

Table 3.8: Thermal evaporation of Silver reservoir

First Photolithography

Notice the baking temperature is very low (Table 3.7). This is because there is already the silver wire on the substrate. It will be definitely damaged if the baking temperature is 95^0C. I have tested baking at different temperatures ranging from 40^0C to 90^0C and found that photo exposure can be successfully done even when the resist is baked at 55^0C for three hours. I used 70^0C for baking the real sample. Before exposing the resist, alignment has to be done so that the normal reservoir will sit on the nanowire. By moving the stage where the substrate sits while watching through the microscope, overlay the alignment marks on the substrate with the marks on the mask. The magnification of the lens is 200X. Before exposing, make sure the resist and the bottom of the mask are in good contact. liftoff time is 30 seconds

Second Photolithography

Conditions are the same as in the first photolithography procedure except that a gentle ion-etching is applied before deposition of the superconducting reservoirs (Aluminum) to ensure good contact between Ag and Al. We used high energy Ar gas to "bombard" the surface of the substrate to remove the dirt before putting

voltage	current	chamber pressure	Ar flow
250 V	10 mA	3×10^{-4} torr	3 sccm

Table 3.9: Ion-milling

metal upon it. The conditions for the ion-etching are in Table 3.9.

The SEM pictures of the sample are shown in figure3.9.

The actual dimensions are given in figure 3.10. The T-shaped Ag wire, $70nm$ wide and $60nm$ thick, is connected to two S reservoirs ($100nm$ of Al) and one N reservoir ($220nm$ of Ag). The distance between S electrodes is $1.1\mu m$, while the distance from the top of the "T" to the N reservoir is $4.5\mu m$.

3.3.3 Method 2: Photolithography First, E-beam Second

Another method starting with photolithography was also used. This is to put down first the SC reservoirs by photolithography. Then, put down the normal wire and the normal reservoir by e-beam alignment and e-beam writing. Most of processes are very similar to the method above except for the e-beam alignment and the ion-etching of the Al surface.

This method requires an extra e-beam process to write down the alignment marks of Au. Note that the Al marks will not be seen because its atomic number is too close to that of Si. The alignment details are given in section 3.2.2.

The ion-etching was difficult because the Al_2O_3 is very hard to remove. This problem was solved by putting an addition Al layer between the copolymer and PMMA so that Al_2O_3 will serve as a mask for etching. This is a rather messy process. It results in a widening of the pattern. Figure 3.11 is a SEM picture of the sample.

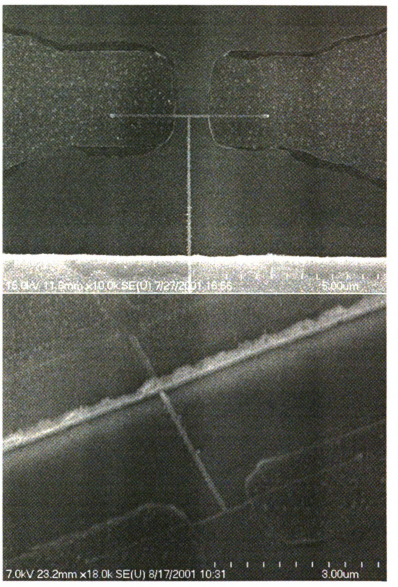

Figure 3.9: SEM pictures of the sample. The upper picture was taken at 10kX and the lower picture was taken at 18kX

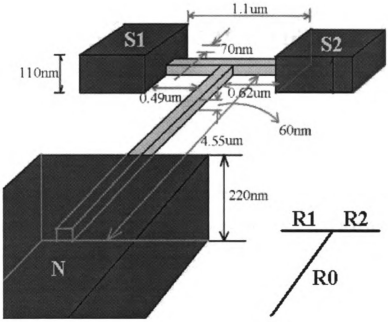

Figure 3.10: The dimensions of the actual sample

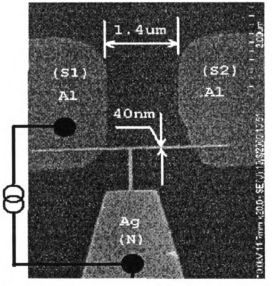

Figure 3.11: SEM picture (taken at 20kX) of the sample by method 2

Chapter 4: Electronics for Measurement

4.1 Sample Mounting

The sample is measured in a mixture of He^4-He^3 in a dilution refrigerator which has a base temperature 28 mK. The sample, which is on a 7mm x 7mm square shaped substrate, is mounted on a sample holder which has a diameter of 12 cm (see Figure 4.1). There are six isolated cells on the holder each of which is covered with Cu sheet. Copper wires are soldered onto each cell, then connected to the sample through Au wires which are fixed by silver paint on the holder and the substrate. There are three current (I) leads (twisted together) for driving currents and there are three voltage (V) leads (also twisted together) for the voltage measurement. Figure 4.2 shows the sample actually sitting on the sample holder. On the substrate, V and I pads alternate. So, the advantage for the design of the holder is that one V lead and one I lead switch sides so that there are no possibilities of crossing the Au wires when connecting them onto the pads.

4.2 Electronics

All electrical leads to the sample are filtered twice - at the top of the cryostat with commercial LC "π" filters with a 3dB roll-off at about 100 MHz, and in the mixing chamber with discrete RC filters with a 3dB roll-off at 160 kHz.

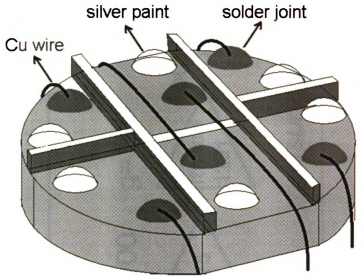

Figure 4.1: Schematics of the sample holder

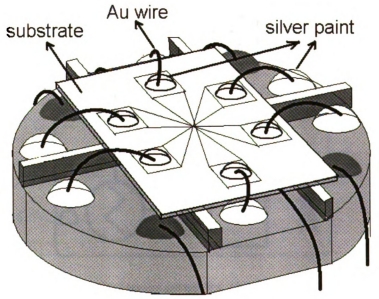

Figure 4.2: Schematics of the sample mounting

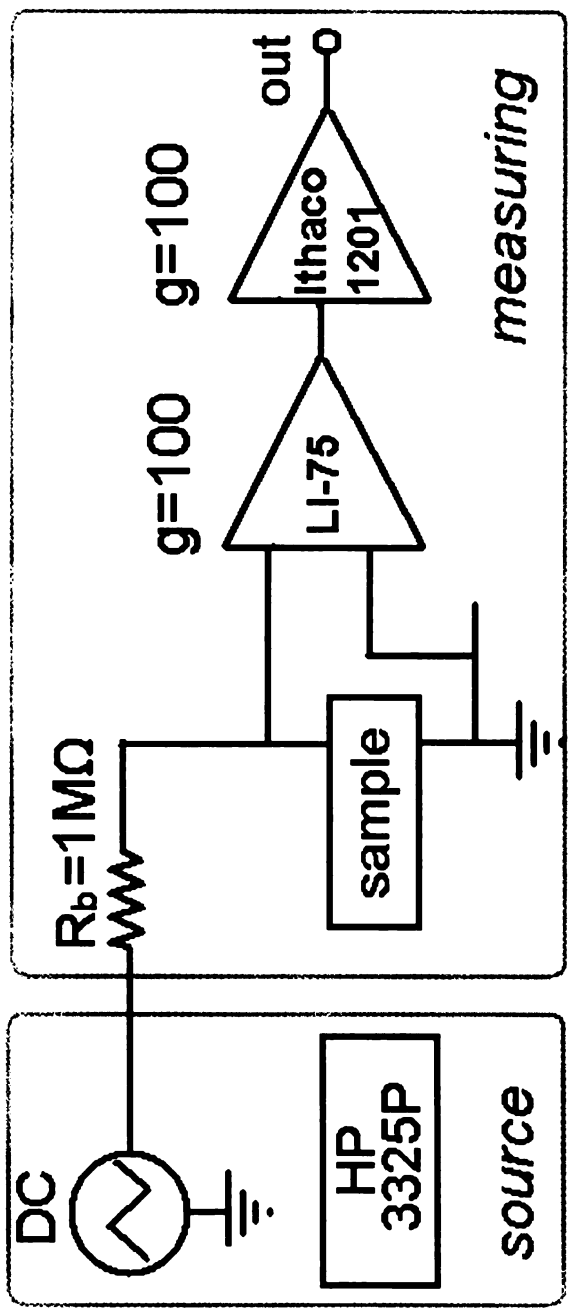

Figure 4.3: electronic setup for the DC measurement

4.2.1 DC Measurement

The setup for the dc measurement is shown in Figure 4.3. The source is a HP function generator. The typical signal used for our measurement has a frequency of 0.01 Hz for the slow dc measurement and 23Hz to 46 Hz for the fast dc averaging measurement. The signal measured from the sample goes through two pre-amps before going into the DMM.

4.2.2 AC Measurement

Summing Box

The driving signal has a fast small ac signal riding upon a slow dc sweeping signal. This is done by using a summing box (see figure 4.4) which has a gain of 0.1 for the dc signal and a gain of 0.01 for the ac signal.

Data Analysis

As shown in figure 4.4, a lock-in amplifier is used to measure the potential change in response to the ac signal. The output is then converted into differential resistance through

$$\frac{dV}{dI} = \frac{V_{Lock-in}}{V_{ac}} * \frac{lock - insensitivity}{10V} * \frac{R_B}{g_{pre-amp}} \tag{4.1}$$

where $V_{Lock-in}$ is the dc voltage at the output of the lock-in amplifier, and V_{ac} is the ac drive signal at the output of the summing box, and R_b is the ballast resistor shown in figure 4.4.

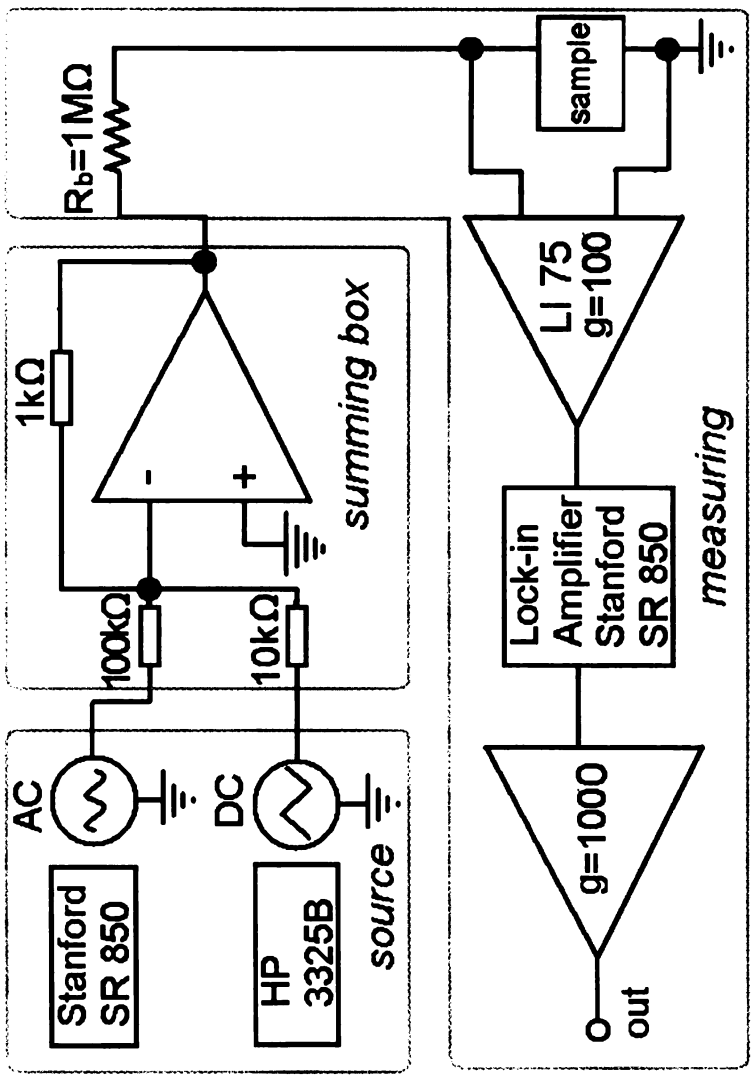

Figure 4.4: Electronic setup for ac measurement

Chapter 5: First Experiment: Dangling Arm

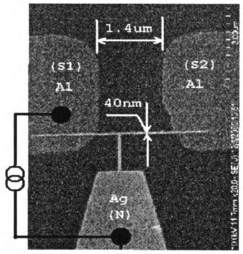

Figure 5.1: SEM picture of the sample

The purpose of this experiment is to test our hypothesis of the counter-flowing quasiparticle current and supercurrent which was discussed in the introduction. To make the discussion easier, let us assume that $R_1 = R_2$ for the moment. If the dc Josephson effect does occur when I_N is less than a critical value $I_C(SN)$, the normal current splits into two going into both superconductors so that the two SC reservoirs are at the same potential. Here, $I_C(SN)$ is defined as the maximum injected current at which the switching from dc Josephson state to the ac Josephson state takes place. So, when $I_N < I_C(SN)$, $I_N \cong 2I_S = 2I_C \sin\phi$, where I_C is the critical supercurrent of the SNS Josepshon junction. The effective resistance between the N reservoir and the left SC reservoir is then $R_{eff} = R_0(\phi) + R_1(\phi)//R_2(\phi)$. When $I_N > I_C(SN)$, the effective resistance will become $R_{eff} = R_0(\phi) + R_1(\phi)$. Notice that the effective resistance depends on the proximity effect which is reflected in the phase difference ϕ. This is why the resistance is written as a function of ϕ.

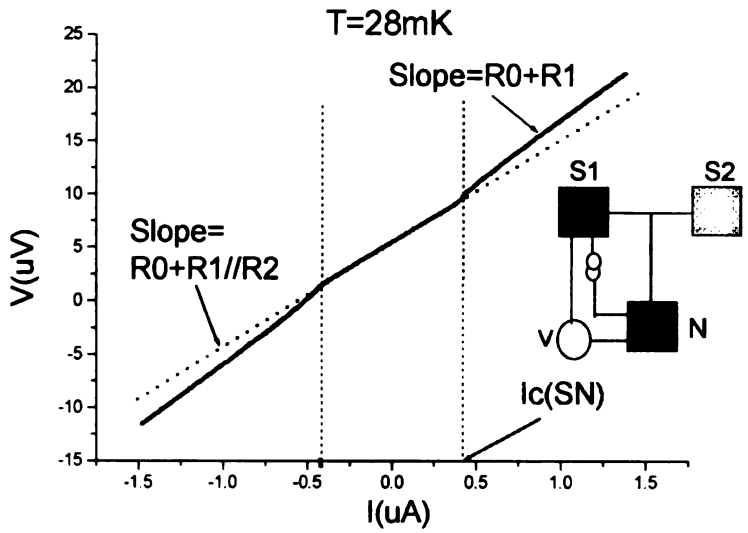

Figure 5.2: DC measurement of V-I

5.1 DC and AC Measurement between the N and S Terminals

The resistances of each arm (R_0, R_1, and R_2) were obtained beforehand by four-terminal measurement at large values of injection current($I_N > I_C(SN)$). The measurement were done between all three pairs of terminals so that we obtained values for $R_0 + R_1$, $R_0 + R_2$, and $R_1 + R_2$. Then, the values for each arm were determined (first three columns in table 5.1).

	R_0	R_1	R_2	$R_0 + R_1//R_2$	$R_0 + R_1$
experiment	7.3Ω	4.0Ω	4.8Ω	9.4 Ω	11.3Ω
prediction base on R_0,R_1,R_2	-	-	-	9.5Ω	-

Table 5.1: Experimental results vs. prediction

The experimental results shown in figure 5.2 are from the dc measurement between the normal terminal and the left superconductor terminal. The data indicates that the effective resistance, which is the slope of the V-I curve, changes when crossing some critical current $I_C(SN)$. Their values agree very well with the

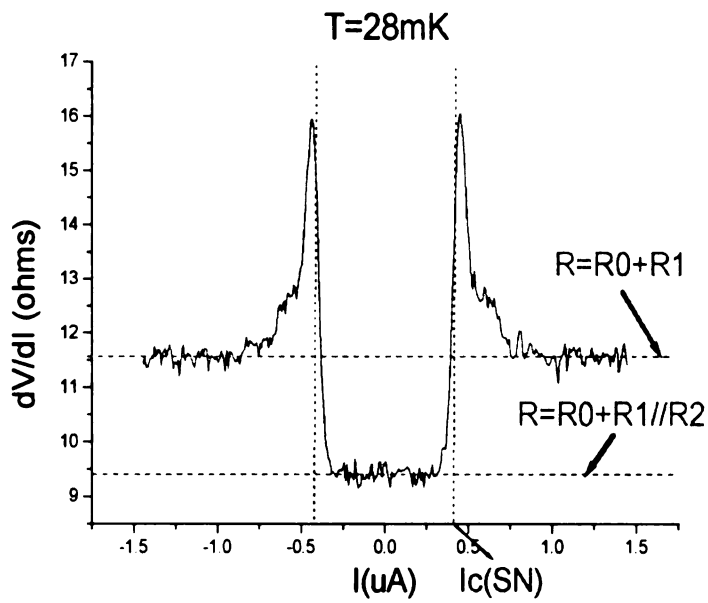

Figure 5.3: AC measurement of (dV/dI) vs. I

prediction base on the values for R_0, R_1, and R_2.(Table 5.1) It convinces us that the effective resistance indeed changes from $R_0(\phi) + R_1(\phi)//R_2(\phi)$ to $R_0(\phi) + R_1(\phi)$ when passing the critical current I_C.

The ac measurement is aimed to reproduce the dc results and to look into more details that the dc measurement might have missed. The data of dV/dI versus I are shown in figure 5.3. The measurement shows a result 9.4Ω for R_{eff} for $I_N < I_C(SN)$ and 11.6Ω for $I_N > I_C(SN)$. Again, they agree very well with the dc measurement. Meanwhile, the ac measurement does reveal some details which the dc measurement did not detect. The switching region from dc Josephson to ac Josephson shows some small oscillations. This may be because a finite potential difference appear introduced by the dramatic change in the resistance so that a small voltage appears when the switching takes place. [29] Also, this also has to do with the fact that the two SN interfaces are not quite the same.

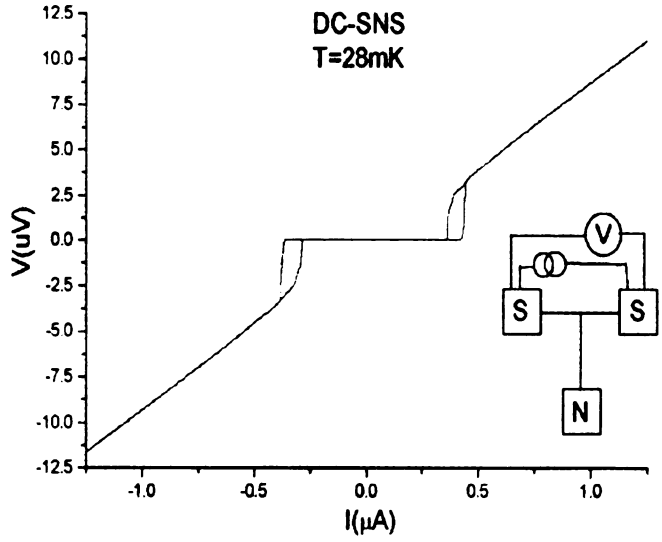

Figure 5.4: DC measurement between the superconducting terminals

5.2 DC and AC Measurement between the S and S Terminals

DC V-I Measurement is also performed between the superconducting terminals (results are shown in figure 5.4). The critical current is then labeled $I_C(SNS)$. The effective resistance is zero when $I_N < I_C(SNS)$ due to the fact that the two S terminals are at the same potential. When $I_N > I_C(SNS)$, it switches to the ac Josephson state. The effective resistance is then $R_{eff} = R_1 + R_2$. We also performed ac measured between S-S terminals and the results are shown in Figure 5.5. Agreeing with the other measurement, it shows that the resistance is zero when $I < I_C(SNS)$, $R_1 + R_2$ when $I > I_C(SNS)$.

5.2.1 Analysis

Both dc and ac results confirmed the fact that the quasiparticle current splits at the cross point. Theoretical analysis of the dangling arm experiment was carried out by Shaikhaidarov et al [30], who performed an experiment similar to ours. The

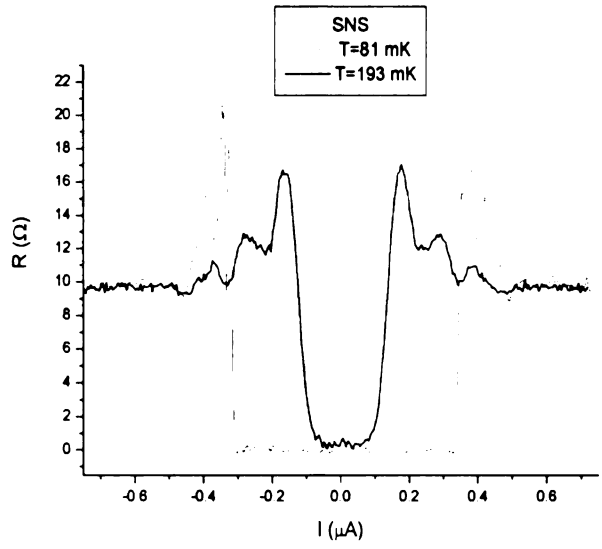

Figure 5.5: AC measurement between the superconducting terminals

resistance, a quantity which is affected by the proximity effect, is phase dependent $R(\phi)$ [30]. Take the effective resistance between the NS terminals $R_{eff}(NS) = R_0(\phi) + R_1(\phi)//R_2(\phi)$ for example, the resistance can be expressed as a normal resistance $R^0_{eff} = R_0 + R_1//R_2$ plus some correction $\delta R cos\phi$ due the proximity effect. So,

$$R_{eff}(NS) = R^0_{eff} - \delta R cos\phi \tag{5.1}$$

where the second term is the proximity contribution. Then, the total normal current in the horizontal arm is

$$I_n = \frac{V_N}{R^0_{eff} - \delta R cos\phi} = \frac{V_N}{R^0_{eff}} \frac{1}{1 - \frac{\delta R}{R^0_{eff}} cos\phi} \tag{5.2}$$

Expand it to the first order, we have

$$I_n = \frac{V_N}{R^0_{eff}} + \frac{V_N}{R^0_{eff}} \frac{\delta R}{R^0_{eff}} cos\phi = 2(I_+ + I_- cos\phi) \tag{5.3}$$

where the factor of 2 arises from the definition of I_+ and I_+. Because $I_N = 2I_S = 2I_C(SNS)\sin\phi$, then,

$$I_C(NS) = (2I_C(SNS)\sin\phi)|_{V=V_{critical}} \tag{5.4}$$

$V_{critical}$ is the maximum applied voltage at which $I_C(NS)$ occurs. In the dangling arm, the total current is

$$I_d = I_C sin\phi - (I_+ + I_- cos\phi) = 0. \tag{5.5}$$

$V_{critical}$ is the maximum value that satisfies the equation above. Putting the $sin\phi$ and $cos\phi$ terms together, we have

$$-I_+ + \sqrt{I_C^2 + I_-^2}\, sin(\phi + \theta) = 0 \tag{5.6}$$

where $cos\theta = I_C/\sqrt{I_C^2 + I_-^2}$. The above equation has a maximum I_+ when $sin(\phi + \theta) = 1$. Because I_+ increases as V_N increases, when I_+ reaches its maximum, V_N reaches $V_{critical}$. So, we have

$$I_+(V_{critical}) = \sqrt{I_C^2(V_{critical}) + I_-^2(V_{critical})} \tag{5.7}$$

Once we have expressions for I_+, I_C, and I_- as functions of V_N, we can solve for $V_{critical}$. So, we obtain

$$sin\phi(V_{critical}) = I_C(V_{critical})/\sqrt{I_C^2(V_{critical}) + I_-^2(V_{critical})} \tag{5.8}$$

which leads to

$$I_C(NS) = 2I_C(V_{critical})^2/\sqrt{I_C^2(V_{critical}) + I_-^2(V_{critical})} \tag{5.9}$$

Notice that $sin\phi(V_{critical})$ can reach 1 only when $I_{-}(V_{critical})$ is negligible, which occurs in the limit of very weak proximity effect.

5.3 Temperature Dependence

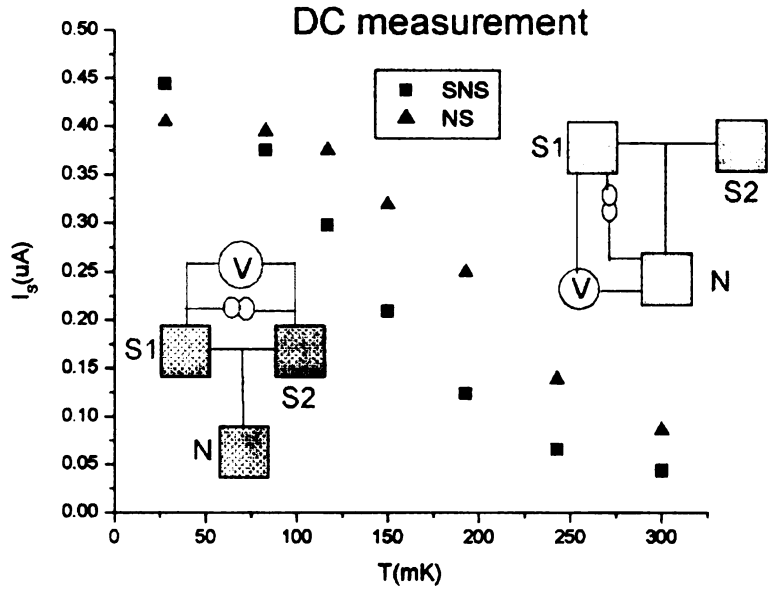

Figure 5.6: Temperature dependence of the critical currents $I_C(SN)$ and $I_C(SNS)$

Figure 5.6 contains two sets of data: $I_C(SNS)vs.T$ (square points) and $I_C(SN)vs.T$ (triangular points). The relationship between them shows to be temperature-dependent. At high temperatures, $I_C(SN) \cong 2I_C(SNS)$. While at lower temperatures, both $I_C(SN)$ and $I_C(SNS)$ increase. Yet, $I_C(SN)$ shows considerable suppression much more than that of $I_C(SNS)$. $I_C(SN)$ even goes below $I_C(SNS)$ at very low temperatures. The reason is that, at low temperatures, the injected normal current can be very high since $I_C(SNS)$ is much larger. The suppression due to the normal current is very high. This is reflected in the rising I_{-} term in equation 5.9 relative to $I_C(SNS)$. When T is high, the injected normal current is limited to a very small value because $I_C(SNS)$ is small. The suppression

due to the quasiparticle injection is buried because the temperature becomes the main factor. The distribution function is indeed affected by both temperature and applied voltage. More discussion will be provided in chapter 6.

5.4 Summary

- The amount of normal injection I_N is limited for the dangling arm case. When the dc Josephson effect takes place, the system responds to the normal injection with a supercurrent $2I_S \cong I_N$. The dc Josephson effect goes away if I_N goes above $2I_C$.

- The supercurrent is a result of the microscopic changes in the distribution function caused by normal current injection. The existence of the net supercurrent indicates that there are more pairs added into the superconductor than being removed at one NS interface while, at the other NS interface, more pairs are removed from the superconductor than being added. This is because that Andreev reflection depends on the available states inside the normal region. The occupation of the states (distribution function) are determined by temperature and injected quasiparticle energy. This will be further discussed in chapter 6 and 7.

Chapter 6: π-Junction

The theoretical discussion of a π junction was provided in chapter 2. In this chapter, our experimental results are presented which followed by more discussions on microscopic interpretation of how π junction appears. Then, rounding factors of the distribution function due to temperature and electron-electron (e-e) interaction is also discussed. Then, a comparison is made with Baselmans' experiment. It ends with the subharmonic gap structures observed in the experiment.

6.1 Observation of the π-Junction

6.1.1 Experiment

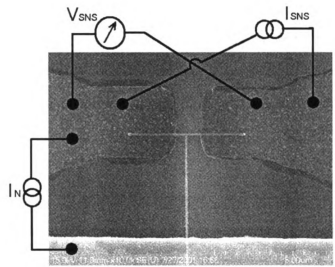

Figure 6.1: SEM picture of the sample and the measurement circuit. The picture is take at 10kX. The distance between S terminals is 1.1μm, and the distance between the cross point and N terminal(bottom of the picture) is 4.5μm

There is a minimum energy that is required for the π junction to take place. This may require the injected current to be much higher than even the critical current I_C. This is impossible for the dangling arm experiment because the dc

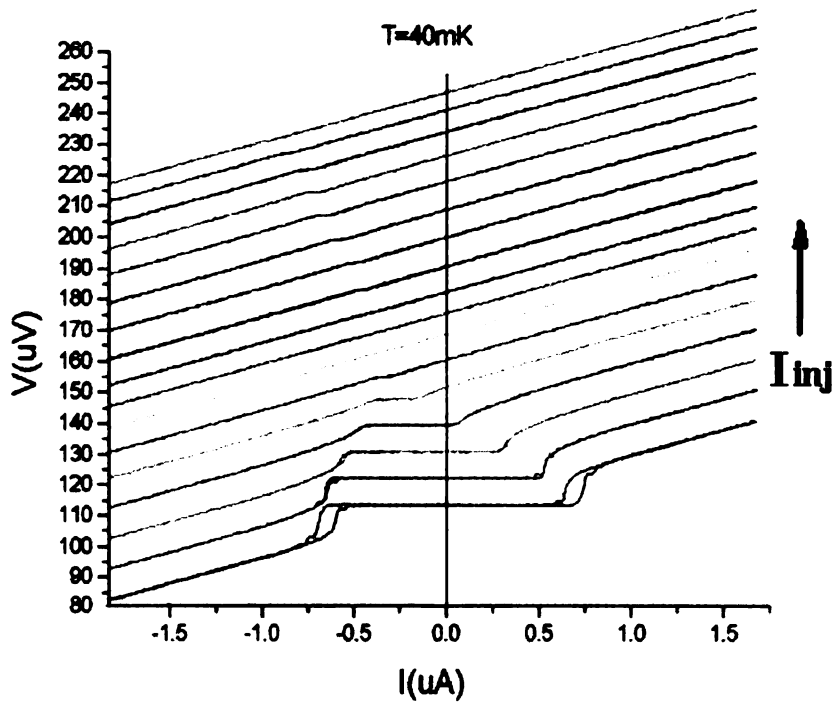

Figure 6.2: dc measurement of the V-I characteristics for different values of I_N

Josephson effect goes away when the I_N exceeds $2I_C$. In order to drive the system farther away from equilibrium, a more general setup shown in figure 6.1 is adopted. The Ag wire has a phase coherence length L_ϕ of several micrometers at sub-Kelvin temperatures, hence we expect to observe a substantial Josephson effect between the two S terminals.

We perform the V-I measurement between the S terminals with the presence of an injected normal current I_N from the normal reservoir. In another words, we sweep the current between the S terminals to determine I_C with each given I_N. We have chosen for I_N the values from $0\mu A$ to $4\mu A$ with steps $0.2\mu A$. The results are shown in figure 6.2 in which each curve corresponds to a fixed value of I_N. The measurement at zero I_N shows a standard Josepshon junction behavior with a critical current $0.76\mu A$. As I_N increases, the critical current $I_C(SNS)$ decreases. [The horizontal shift of the curves is due to the asymmetric injection]. A selected subset of the curves from figure 6.2 are magnified in figure 6.3

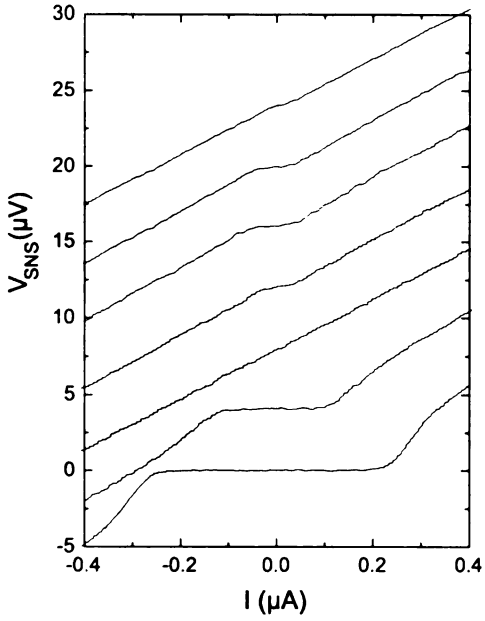

Figure 6.3: Selected curves from the previous graph for following values of I_N: 0.53, 0.70, 1.01, 1.23, 1.89, 2.18, 3.15 μA

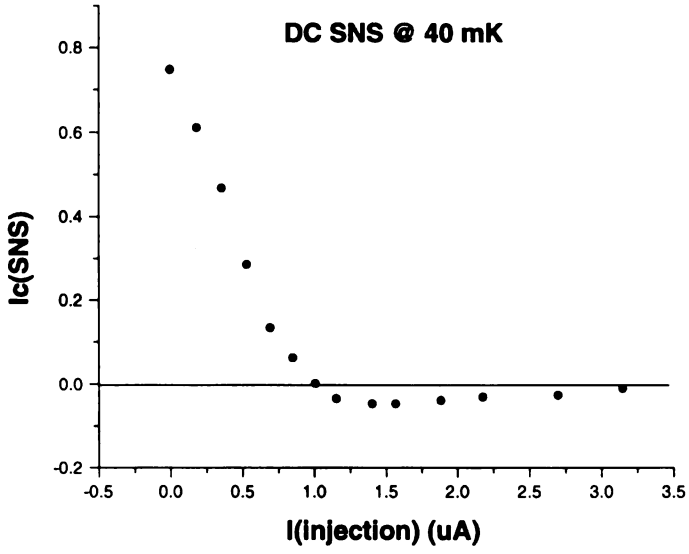

Figure 6.4: $I_C(SNS) vs. I_{inj}$ at 40 mK

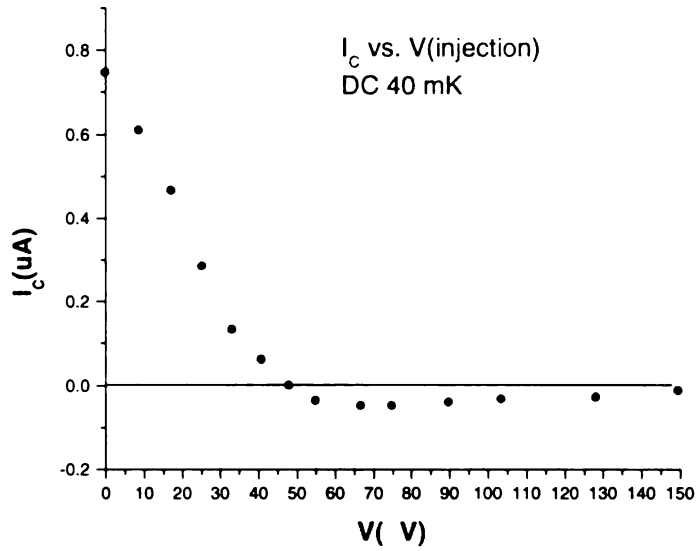

Figure 6.5: I_C vs. V_{inj}

By measuring the I_C in figure 6.2, we obtained I_C vs. I_N which is shown in figure 6.4. Multiplying I_N by the effective resistance, $I_C(SNS)$ vs. V_{inj} is also obtained (figure 6.5). The critical current decreases to zero when I_N reaches $1.0\mu A$. The corresponding energy is $\sim 48\mu V$. As I_N continues to increase, the critical current reaches a local maximum at $I_N \sim 1.5\mu A$ which corresponds an energy $\sim 65\mu V$. Finally, I_C goes to zero at large injection. This behavior of I_C is, as will be discussed later, a signature of the π junction. Note I_C is the maximum current that the Josephson junction allows to pass. It should always be positive because it is an absolute value. In order to show the sign reversal of the supercurrent, we purposely plotted I_C as negative after it reaches zero for the first time. The π junction appears when the dominant occupation of the energy states changes from one direction to the other.

6.1.2 Discussion on the appearance of π junction

As discussed in chapter 2, the appearance of the π junction is controlled by controlling the width of the staircase distribution function f_0 which is $2eV$ (from $-eV$ to eV). (see figure 2.12) This determines which energy states exist in the supercurrent energy spectrum. Then, the sign of the integrand of the net supercurrent

$$I_S = (\sigma_N/2) \int d\varepsilon Im[j(\varepsilon)] f_0(\varepsilon) \tag{6.1}$$

depends on the value of eV. For $eV_N < E_0$, the junction is at zero phase state(the sign of the product of f_0 and $Im[j(E)]$ is positive); for $eV_N \sim E_0$, I_C goes to zero; and for $eV_N > E_0$, π phase state appears (the sign of the product of f_0 and $Im[j(E)]$ is negative). As discussed in chapter 2, the antisymmetric distribution function f_0 and symmetric distribution function f_1 are coupled through $Im[j(E)]$. The exact relations are shown in two coupled equations which are derived from the Keldysh part of the Usadel equation [31] (refer to chapter 7).

$$\nabla j^C(E) = \nabla(D_1 \nabla f_1) + 2Im[j(E)]\nabla f_0 = 2\frac{R}{D} f_1 \tag{6.2}$$

and

$$\nabla j^Q(E) = \nabla(D_0 \nabla f_0) + 2Im[j(E)]\nabla f_T = 0 \tag{6.3}$$

$j^C(E)$ is the charge current density and $j^Q(E)$ is the heat current density.

$Im[j(E)]$ is the spectral supercurrent density, D_0 and D_1 are the diffusion constants for heat and charge diffusion. R, the contribution due to the gap, is the zero in the normal metal. $j^C(E)$, a constant through out the normal wire, includes both normal current part and supercurrent part.

$$j_S = \frac{\sigma_N}{2} \int dE Im[j(E)] f_0 \tag{6.4}$$

and

$$j_N = \frac{\sigma_N}{2} \int dE D_1 (\nabla f_1) \tag{6.5}$$

When ϕ is zero, $Im[j(E)] = 0$. The two equations are decoupled. When $\phi \neq 0$, they are coupled in a more complicated way. A simplification occurs in the vertical arm of the sample. First, the heat current $j^Q(E)$ can not exist for energies less than Δ because Andreev reflection does not allow heat transfer through the NS interface. Because the vertical arm has a constant ϕ, the supercurrent density is zero in that arm. So, equation 6.3 leads to a constant f_0 in the vertical arm. Thus, Equation 6.3 then leads to a constant f_0. So, f_0 at the cross point takes the value of f_0 in the normal reservoir:

$$f_0^0 = \frac{1}{2}[tanh\frac{E+eV}{2k_BT} + tanh\frac{E-eV}{2k_BT}] \tag{6.6}$$

6.2 π-Junction affected by the rounding of f_0

There are two processes that lead to the rounding of f_0 which suppresses I_C [32]: temperature and local heating caused by electron-electron interaction.

6.2.1 Temperature

The dc measurements were performed at fridge temperatures 40 mK, 96 mK, 154 mK, 200 mK, 244 mK, and 304 mK. (data for 96mK, 200mK, and 304mK are shown in figure 6.7. It is extrapolated that the π junction disappears around 350 mK. This corresponds to 55 μV which is around the quasiparticle energy at which π junction appears. The I_C vs. I_{inj} and I_C vs. V_{inj} are also plotted for the three temperatures in figure 6.8. At very low temperature close to $T = 0$, the step shape

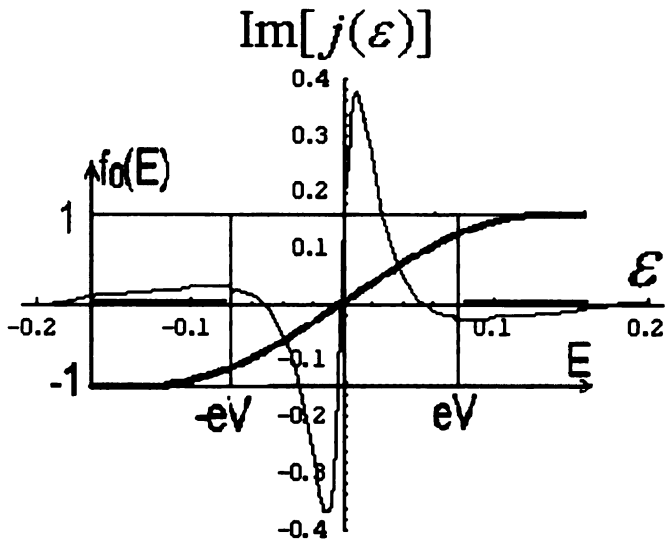

Figure 6.6: Absence of the π junction resulted from the rounding of the distribution function due to the increase of temperature

of the distribution function is maintained because the energy of each quasiparticle is conserved. When T increases, the distribution function becomes more and more rounded until the integration of the product of $Im[j(E)]$ and f_0 can no longer be negative(see figure 6.6). Then, the π phase shift can no longer be observed. Another factor that contributes to the temperature of the system is the reservoir heating [33]. Due to the very high heat impedance at the NS interface, the heat carried by the injected quasiparticles has to be removed by the normal reservoir to avoid heating in the wire. So, one has to increase the electron-phonon interaction inside the normal reservoir so that the heat is carried away efficiently. The effective cooling by electron-phonon interaction is proportional to the volume of the normal metal. This is why we fabricated a $220nm$ thick normal reservoir in which the estimated heating is about 1K/mV.

6.2.2 e^-e^- interaction

The energy of the injected quasiparticles not only determines the width of the staircase of f_0, but also brings rounding effect to f_0. This is because, as discussed in

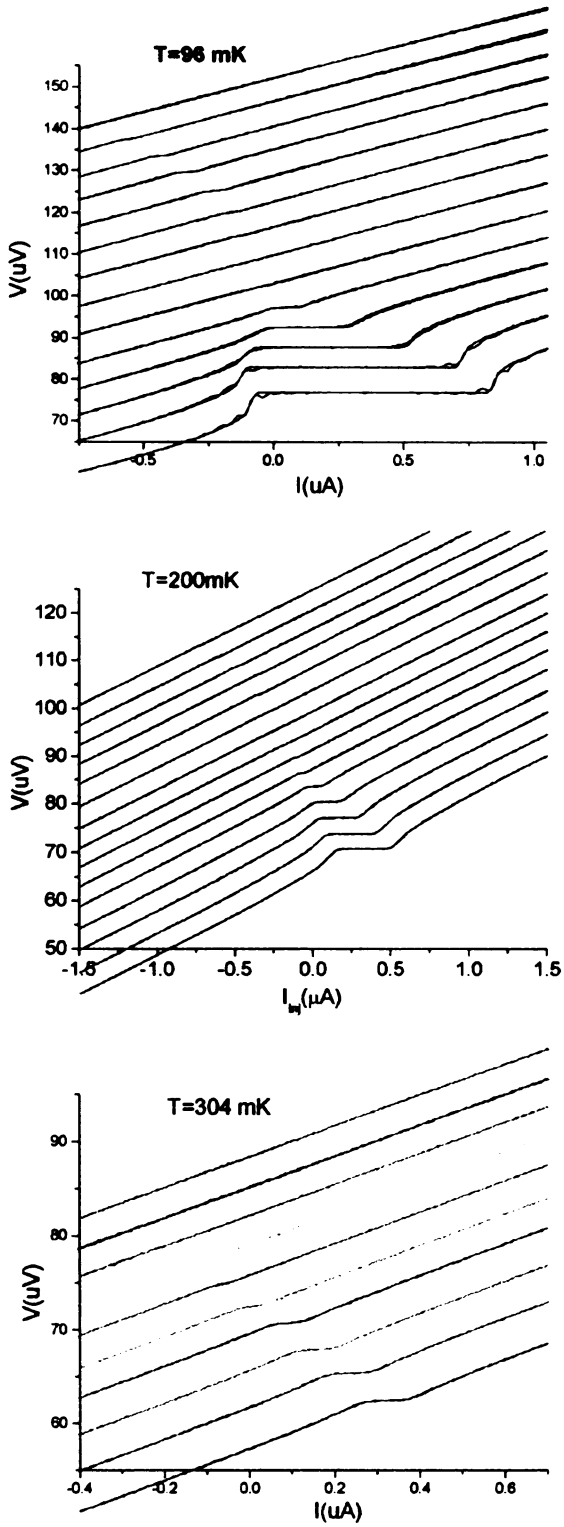

Figure 6.7: V-I characteristics for 96mK, 200mK, and 304mK

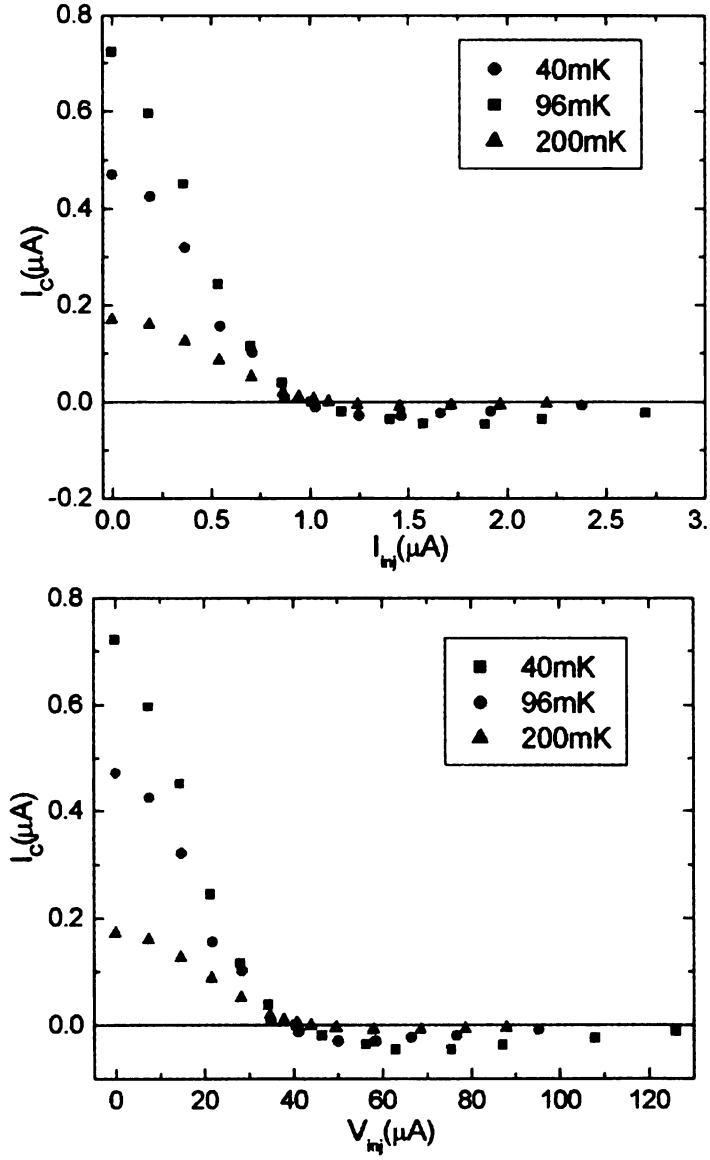

Figure 6.8: I_C vs. I_{inj} and I_C vs. V_{inj} for 96mK, 200mK, and 304mK

chapter 2, ee inelastic collisions brings energy exchanges among the electrons and results in local heating of the electrons which can be much higher than the lattice temperature. This heating becomes another factor that causes the rounding of f_0. We can calculate the shape of the distribution function by solving the Boltzmann's equation in the diffusive limit [34]

$$\frac{1}{\tau_D}\frac{\partial^2 f(x,E)}{\partial x^2} + I_{coll}(x,E) = 0 \tag{6.7}$$

where the inelastic collision contribution is expressed as

$$I_{coll}(x,E) = I^{in}_{coll}(x,E) - I^{out}_{coll}(x,E) \tag{6.8}$$

And,

$$I^{in}_{coll}(x,E) = \int d\varepsilon dE\prime f(x,E+\varepsilon)(1-f(x,E)) \times \kappa(\varepsilon) f(E')(1-f(x,E\prime+\varepsilon) \tag{6.9}$$

and

$$I^{out}_{coll}(x,E) = \int d\varepsilon dE\prime f(x,E)(1-f(x,E-\varepsilon)) \times \kappa(\varepsilon) f(E')(1-f(x,E\prime+\varepsilon) \tag{6.10}$$

$\kappa(\varepsilon)$ is called the interaction kernel which depends on the exchange energy ε. The calculation of $\kappa(\varepsilon)$ in a diffusive wire was done by Altshuler in 1980 [35]. He used Fermi's Golden rule with corrected potential due to polaron and diffusion process and obtained

$$\kappa(\varepsilon) = \kappa_{3/2}\varepsilon^{-3/2} \tag{6.11}$$

where $\kappa_{3/2} = (\sqrt{D/2}\pi\hbar^{3/2}v_F A)^{-1}$. A is the cross section of the wire. Whether or not this scattering plays a big effect depends on how the scattering time τ_E (inverse of the scattering rate Γ_E) is compared to the diffusion time τ_D.

$\tau_D = 4(L_S/2 + L_N)^2/D$, where $D = 150cm^2/s$ is the diffusion constant, L_S(half of the length between S terminals) is $0.5\mu m$, and L_N (length of the vertical arm) is $4.5\mu m$. This gives 6ns for the τ_D. The scattering time can be approximated as $1/\Gamma_E$ where $\Gamma_E = (1/2)k_{3/2}\sqrt{E - eV}$. $k_{3/2} \approx 0.5ns^{-1}meV^{-1/2}$ is an approximation of $\kappa(\varepsilon)$ for low energies. For $eV = 0.05meV$, one has 3ns for τ_E. So, because of the long vertical arm, electron-electron interaction should be taken into consideration. Using a program written by Frederic Pierre during his Ph.D thesis, we have solve equation 6.7 numerically for our sample to determine the rounding of the distribution function f_E.

6.3 Comparison with Baselmans' Experiment

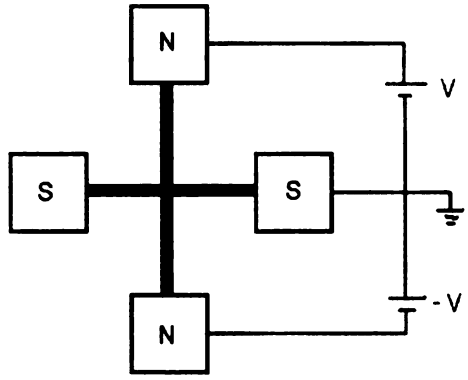

Figure 6.9: Schematic picture of Baselmann's four terminal device and measurement setup [1]

Baselmans et al [1] [36] used a four-terminal device shown in figure 6.9 with two S and two N electrodes. The normal current is injected from one N reservoir to the other by putting $2V$ voltage difference between them. They have measured the V-I characteristic between the two S terminals of which the results are shown in figure 6.10. The effective resistance $R_{eff}(SN)$ between the S and N terminals is also measured at both zero phase state and the π phase state. The change of the resistance $\Delta R_{eff}(SN)$ depends on how strong the proximity effect is. At zero phase

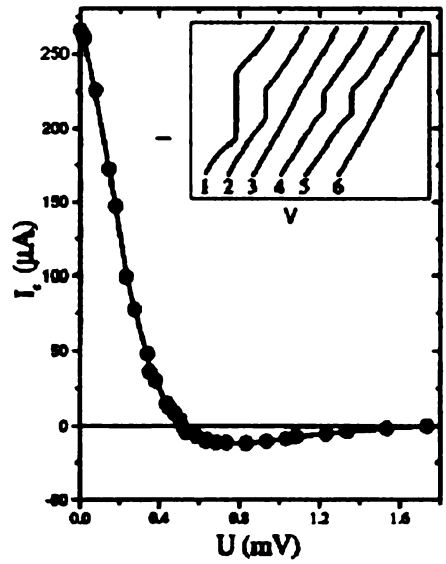

Figure 6.10: Observed π junction and I_C vs. $V_{control}$ in Baselmans et al's experiment [1]

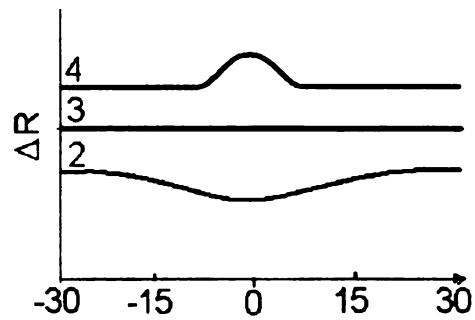

Figure 6.11: Difference of changes of $R_{eff}(SN)$ at zero phase state and π state

state, the $\Delta R_{eff}(SN)$ reaches its minimum for $I_{SNS} = 0$ because the proximity is the strongest. With the same situation in the π state, $\Delta R_{eff}(SN)$ reaches its maximum because the proximity effect is the weakest. The differences in $\Delta R_{eff}(SN)$ is the direct indication that the π phase state indeed occurs. This lays the foundation for our statement earlier about the signature of π junction.

In the horizontal arm of Baselmann's four terminal device, there is no normal current flowing even though there are normal quasiparticles present. The quasiparticles are not current carrying states, so the normal current

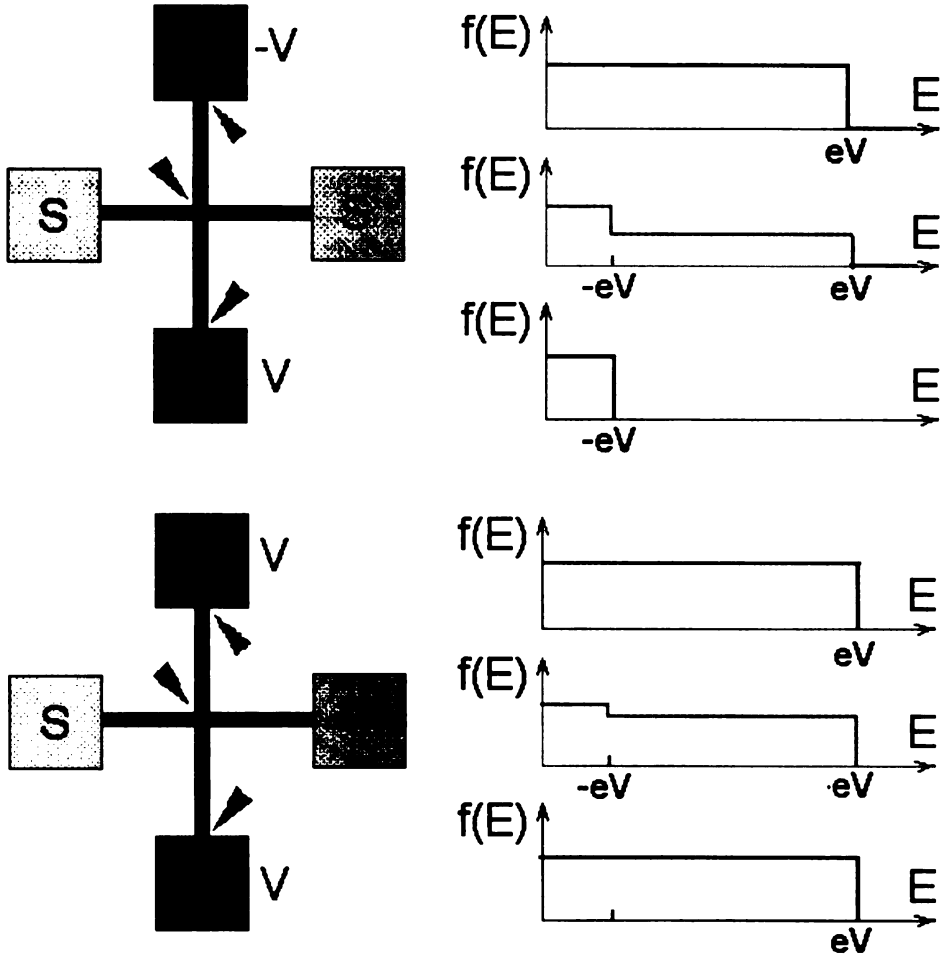

Figure 6.12: Comparison of the total distribution functions between baselmans' device (top) and a four-terminal device with current flow equivalent to that in our device (bottom)

quasiparticles are not current carrying states, so the normal current

$$j_N = \frac{\sigma_N}{2} \int dE D_1 (\nabla f_1) = 0 \tag{6.12}$$

A comparison of the total distribution functions is shown in figure 6.12 In our three terminal case, normal current does appear inside the horizontal arm so that f_0 and f_1 are more complicated coupled than the four-terminal case. The net momentum of the quasiparticles is due to the finite potential at the cross point. While, in Baselmann's setup, the potential is zero at the cross point. So, the scattering of the Cooper pair-like states due to the normal injection is different for the two setups because of the difference in quasiparticle states. [37]

6.4 Sub-harmonic Gap Structure

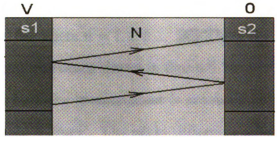

Figure 6.13: Schematic picture of multi-Andreev processes

Sub-harmonic Gap Structure(SGS) is an amplified normal conductance related to the multi-Andreev processes(figure 6.13). It only happens when there is a finite potential difference between the SC reservoirs($I_N < I_C$). After a particle is reflected as a hole at the NS interface, it travels to the other NS and gets reflected as an electron again. During this propagation, the hole gains eV. (V is the potential difference). And, this electron travels back and gets reflected again. The energy of the particle keeps increasing as it travels back and forth. Until, after nth reflection,

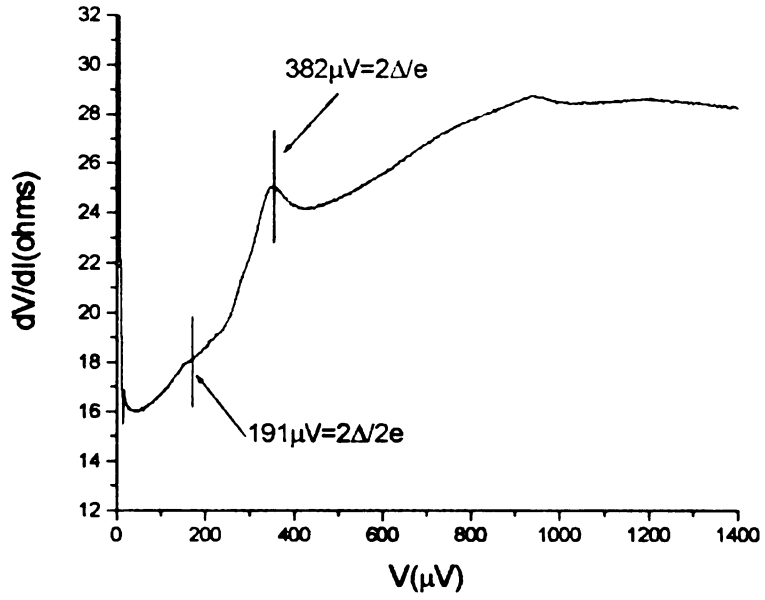

Figure 6.14: Observation of the Sub-harmonic Gap Structure

the particle has enough energy overcoming the gap of the superconductor, it goes into the superconductor and becomes a superconducting excitation after a charge relaxation time. Actually, this single particle tunnelling happens at the fractions of the gap voltage $(2\Delta/e)/n$, where $n = 1, 2, 3....$ [38] These correspond to the peaks of the measured differential resistance shown in figure 6.14.

The gap obtained from the measurement is around $0.191meV$. The typical value for the gap is about $0.2meV$. The slight difference is ascribed to the presence of the normal metal surrounding the SC reservoirs.

Chapter 7: Quasiclassical Theory

7.1 Review of the quasiclassical formalism

There are several excellent review articles on this topic. The review by Rammer and Smith [39] (1986) provides great details. This thesis follows closely the review by Lambert and Raimondi [40](1998) which follows mainly Larkin and Ovchinnikov's (1986) approach [41].

The quasi-classical approach to the theory of superconductivity was first initiated by Eilenberger(1968) [42] who applied Gorkov's equation to the dirty limit. This method was further developed by Larkin and Ovchinnkov (1969), Usadel [43] (1970), Eliashberg (1971), Larkin and Ovchinnikov (1973, 1975), and has been largely used to analyze transport phenomena in dirty hybrid systems. In contrast with the BdG equations, this approach, due to its diffusion-like nature, can be used on scales significantly exceeding the Fermi wavelength $\lambda_F = 2\pi/k_F$, and even the elastic main free path l. The following is a brief review of the quasi-classical Green's functions approach.

It is convenient to express the Green functions in matrix form with the matrix elements being the ordinary and anomalous Green functions

$$i\hat{G}^{>}(1,2) = \begin{pmatrix} \langle \psi_\uparrow(1)\psi_\uparrow^+(2)\rangle & \langle \psi_\uparrow(1)\psi_\downarrow(2)\rangle \\ -\langle \psi_\downarrow^+(1)\psi_\uparrow^+(2)\rangle & -\langle \psi_\downarrow^+(1)\psi_\downarrow(2)\rangle \end{pmatrix} \tag{7.1}$$

and

$$i\hat{G}^{<}(1,2) = \begin{pmatrix} \langle \psi_\uparrow^+(2)\psi_\uparrow(1)\rangle & \langle \psi_\uparrow(2)\psi_\downarrow(1)\rangle \\ -\langle \psi_\downarrow^+(2)\psi_\uparrow^+(1)\rangle & -\langle \psi_\downarrow^+(2)\psi_\downarrow(1)\rangle \end{pmatrix} \tag{7.2}$$

Where $1 \equiv (r_1, t_1)$, and $2 \equiv (r_2, t_2)$. Following from the Keldysh formalism, in the Nambu space [44] where the spinor operators

$$\Psi(r) = \begin{pmatrix} \psi_\uparrow(r) \\ \psi_\downarrow^+(r) \end{pmatrix} \tag{7.3}$$

$$\Psi^+(r) = \begin{pmatrix} \psi_\uparrow^+(r) & \psi_\downarrow(r) \end{pmatrix} \tag{7.4}$$

are introduced to treat the pairing, the advanced, retarded, and Keldysh matrices of Green's functions [45] [46] are defined

$$\hat{G}^R(1,2) = \theta(t_1 - t_2)[\hat{G}^>(1,2) - \hat{G}^<(1,2)] \tag{7.5}$$

$$\hat{G}^A(1,2) = -\theta(t_2 - t_1)[\hat{G}^>(1,2) - \hat{G}^<(1,2)] \tag{7.6}$$

$$\hat{G}^K(1,2) = \hat{G}^>(1,2) + \hat{G}^<(1,2) \tag{7.7}$$

These can also be written as $\hat{G}^{R/A} = G^{R/A}\hat{\sigma}_z + \hat{F}^{R/A} = G^R\hat{\sigma}_z + i(\hat{\sigma}_x F_x^{R/A} + \hat{\sigma}_y F_y^{R/A})$ and $\hat{G}^K = \hat{G}^R\hat{f} - \hat{f}\hat{G}^A$, where G and F are the Gorkov normal and condensate amplitudes and $\hat{f}$ is the filling matrix. Now, the system can be written as

$$\check{G} = \begin{pmatrix} \hat{G}^R & \hat{G}^K \\ 0 & \hat{G}^A \end{pmatrix} \tag{7.8}$$

and the $\check{\Sigma}$ is the matrix of self-energies with retarded, advanced, and Keldysh parts

$$\check{\Sigma} = \begin{pmatrix} \hat{\Sigma}^R & \hat{\Sigma}^K \\ 0 & \hat{\Sigma}^A \end{pmatrix} \tag{7.9}$$

They satisfy the nonequilibrium Dyson equation

$$(\check{G}_0^{-1} - \check{\Sigma})\check{G} = \check{1} \tag{7.10}$$

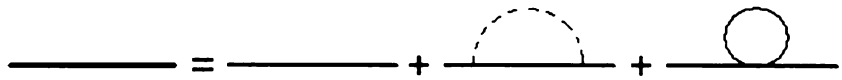

Figure 7.1: The diagram equation for Green's functions

and its conjugate equation

$$\check{G}(\check{G}_0^{-1} - \check{\Sigma}) = \check{1} \tag{7.11}$$

To cancel the large terms, one takes the difference between the two equations

$$\left[\check{G}_0^{-1} - \check{\Sigma}, \check{G}\right] = 0 \tag{7.12}$$

The equations for $\check{G}$ averaged over realizations of the elastic scattering potential is given by the diagram shown in figure 7.1 [47]. For the diffusion case in which the spatial scale is much larger than the mean free path, it can be integrated over $\xi = p^2/2m - \mu$ because only $\check{G}$ now has the sharp dependence on p^2. This equation is simplified by going to the center of mass and relative coordinates (R, T) and (r, t) defined as

$$r_{1,2} = R \pm r/2 \qquad\qquad t_{1,2} = T \pm t/2$$

and Fourier transforming with respect to r and t, and introducing the quasi-classical Green's function defined by

$$\check{g}(R, T; \hat{p}, \epsilon) = \frac{i}{\pi} \int_{-\infty}^{+\infty} d\xi \; \check{G}(R, T; p, \epsilon) \tag{7.13}$$

where $\xi = p^2/2m - \mu$ is the energy measured from the Fermi level and $\hat{p}$ is the unit vector in the direction of the momentum p. With the assumption that the self-energy depends weakly on the energy ξ, one sets $\xi = 0$ in $\check{\Sigma}$, which yields

$$\partial_T \left\{\check{\tau}_z, \check{g}\right\} + v_F \, \hat{p} \cdot \partial_R \check{g} - i\epsilon \left[\check{\Sigma}, \check{g}\right] = 0 \tag{7.14}$$

This is basically the equation for the quasi-classical Green's function derived by Eilenberger. $\check{\tau}_z$ is a block-diagonal matrix with diagonal block entries $\hat{\sigma}_z$. The normalization condition is

$$\check{g}\check{g} = 1 \tag{7.15}$$

In the dirty limit, the effect of non-magnetic impurities can be described by the self-energy

$$\check{\Sigma} = -\frac{i}{2\tau}\langle\check{g}\rangle \tag{7.16}$$

and the equation was considerably simplified by Usadel who expanded $\check{g}$ in spherical harmonics keeping the only the s-wave and p-wave terms:

$$\check{g}(\cos(\theta)) = \check{g}_0 + \cos(\theta)\check{g}_1 \tag{7.17}$$

with $\check{g}_0$ and $\check{g}_1$ not depending on $\cos(\theta)$ and $\cos(\theta)\check{g}_1 \ll \check{g}_0$. Now insert the above equation into equation 7.14, and with $\check{g}_1$ expressed in terms of $\check{g}_0$,

$$\check{g}_1 = -l\check{g}_0\partial_R\check{g}_0 \tag{7.18}$$

where $l = v_F\tau$ is the mean free path. For $\check{g}_0$ one obtains a diffusion-like equation:

$$D\ \partial_R\check{g}_0\partial_R\check{g}_0 + i\epsilon\left[\check{\sigma}_z, \check{g}_0\right] - \partial_T\left\{\check{\sigma}_z, \check{g}_0\right\} = 0 \tag{7.19}$$

with $D = v_F l\tau/3$ the diffusion coefficient. The first term is the variation of $\check{g}_0$, the second term is the energy, and the third term is due to the inelastic scattering which can also be written as $(\gamma/2)\left[\check{\sigma}_z\ \check{g}_0\ \check{\sigma}_z,\ \check{g}_0\right]$ where γ is the inelastic scattering rate. Then, writing $\check{g}_0$ as $\check{g}$, one has

$$D\ \nabla(\check{g}\nabla\check{g}) + i\varepsilon\left[\check{\sigma}_z, \check{g}\right] - (\gamma_N/2)\left[\check{\sigma}_z\ \check{g}\ \check{\sigma}_z,\ \check{g}\right] = 0 \tag{7.20}$$

Practically, the equation has to be solved in the presence of boundary conditions contributed by the work of Zaitsev [48]

$$\check{I} = \frac{\sigma}{e}\check{g}_{2S}\partial_R\check{g}_{2S} = \frac{G_T}{2e}\left[\check{g}_{2S}, \check{g}_{1S}\right] \tag{7.21}$$

where "s" refer to the symmetric part of the Green's funtion matrices.

For tunnel junctions (see AppendixA), with the boundary conditions shown above, the tunnel current is

$$j = \frac{G_T}{8e}\int_{-\infty}^{+\infty} d\epsilon (I_J + I_{PI}) \tag{7.22}$$

where

$$I_J = i\sin(\phi)[f_2^0(F_2^R - F_2^A)(F_1^R + F_1^A) + f_1^0(F_2^R + F_2^A)(F_1^R - F_1^A)] \tag{7.23}$$

and

$$I_{PI} = [(G_1^R - G_1^A)(G_2^R - G_2^A) + \cos(\phi)(F_2^R + F_2^A)(F_1^R + F_1^A)](f_1^Z - f_2^Z)] \tag{7.24}$$

I_J is the Josephson current, while I_{PI} is sometimes referred to as the quasi-particle and interference current. The detailed derivation is provided in the appendix A.

Things get more complicated when solving the quasiclassical equation in a diffusive region (see also AppendixC). The components of the diffusion-like equation have the diagonal part

$$\partial_R(\hat{g}^{R(A)}\partial_R\hat{g}^{R(A)}) = i\epsilon[\hat{\sigma}_Z, \hat{g}^{R(A)}] + (\gamma_N/2)\left[\check{\sigma}_z\ \check{g}\ \check{\sigma}_z,\ \check{g}\right] \tag{7.25}$$

which describes the energy spectrum of the states and the Keldysh part

$$\partial_R(\hat{g}^R\partial_R\hat{g} + \hat{g}\partial_R\hat{g}^A) = 0 \tag{7.26}$$

which describes the occupation of these states. The first equation gives the energy spectrum. Using $\hat{g} = \hat{g}^R\hat{f} - \hat{f}\hat{g}^A$(result from the normalization condition) and the equation for $\hat{g}^{R(A)}$, the equation for the Keldysh part becomes

$$\partial_R[\partial_R\hat{f} - \hat{g}^R(\partial_R\hat{f})\hat{g}^A] - (\hat{g}^R\partial_R\hat{g}^R)(\partial_R\hat{f}) - (\partial_R\hat{f})(\hat{g}^A\partial_R\hat{g}^A) = 0 \tag{7.27}$$

$\hat{f} = f_0\hat{\sigma}_0 + f_1\hat{\sigma}_Z$ is the filling matrix or matrix for the distribution functions. f_0 is the asymmetric part which reflects the effective temperature, and f_1 is the symmetric part which reflects the chemical potential change. For NS systems, the equation becomes easier to solve because $\hat{g}^R = G^R\hat{\sigma}_Z + iF^R\hat{\sigma}_y$ which does not have superconducting phase variance. The Keldysh part of the equations becomes

$$\partial_R[(1 - G^RG^A - F^RF^A)\partial_Rf_1] = 0 \tag{7.28}$$

But, for the SNS systems, both the amplitude and the phase of the Green's functions inside the normal region are complex. The Keldysh part gives the supercurrent and normal current components

$$I_S = \frac{\sigma_N}{8}\int Tr\hat{\sigma}_Z[\hat{F}^R\partial\hat{F}^R - \hat{F}^A\partial\hat{F}^A]f_0dE \tag{7.29}$$

and

$$I_N = \frac{\sigma_N}{8}\int Tr\hat{\sigma}_Z[1 - G^RG^A + \hat{F}^R\hat{F}^A]\hat{\sigma}_Z(\partial f_1)dE \tag{7.30}$$

where I_S is the supercurrent and I_N is the normal current. Another equivalent way

to express the currents follows from converting the Keldysh equation into a pair of equations [31]

$$\nabla(D_1\nabla f_1) + 2\,\mathrm{Im}[j(E)]\nabla f_0 = 2\frac{R}{D}f_1 \tag{7.31}$$

and

$$\nabla(D_0\nabla f_0) + 2\,\mathrm{Im}[j(E)]\nabla f_T = 0 \tag{7.32}$$

where

$$2\,\mathrm{Im}[j(E)] = (1/4)Tr\hat{\sigma}_Z[\hat{g}^R\partial\hat{g}^R - \hat{g}^A\partial\hat{g}^A] \tag{7.33}$$

is the spectral supercurrent density, and

$$D_0 = (1/4)Tr(\hat{g}^R\hat{g}^A) \tag{7.34}$$

$$D_1 = (1/4)Tr(1 - \hat{g}^R\hat{\sigma}_Z\hat{g}^A\hat{\sigma}_Z) \tag{7.35}$$

$$R = (1/4)Tr\hat{\Delta}(\hat{g}^R + \hat{g}^A) \tag{7.36}$$

D_0 and D_1, affected by the proximity effect, are the energy-dependent diffusion coefficients for heat diffusion and charge diffusion. The current densities are

$$j_S = \frac{\sigma_N}{2}\int dE\,\mathrm{Im}[j(E)]f_0 \tag{7.37}$$

and

$$j_N = \frac{\sigma_N}{2}\int dE D_1(\nabla f_1) \tag{7.38}$$

The R in equation 7.31 is zero for the normal region it becomes the conservation of the total charge current. Similarly, equation 7.32 represents the conservation of the thermal current.

[Note: The Usadel equation can be written (often more convenient) in terms of

the amplitude and phase of the Green's functions θ and ϕ both of which are complex in the normal region of a SN device. [49]]

7.2 Analytical Solution with High-barrier Approximation

The Usadel equation is highly nonlinear so it is very difficult to solve analytically. So, we adopt the way of linearizing the Usadel equation with high-barrier approximation developed by Volkov. [50] [51] [52] [53] [54] When the barrier resistance of the NS interface is much higher than the resistance of the normal metal, the solutions for the Green's functions have the form

$$\hat{F}^{R(A)} = \pm i(\varepsilon_1 \hat{F}_{S1}^{R(A)} + \varepsilon_2 \hat{F}_{S2}^{R(A)})/(\varepsilon + i\gamma) \tag{7.39}$$

The details of the calculations are provided in Appendix B.

When the resistance of the interface $R_{S/N}$ is comparable to the normal wire resistance R_N, the solutions above are not valid. But, the Usadel equation can be linearized by using $F^R = \sinh u^R \approx u^R$. Then, the diagonal part of the Usadel equation becomes

$$\partial_{xx}\hat{F}^{R(A)} - (k^{R(A)})^2 \hat{F}^{R(A)} = 0 \tag{7.40}$$

$(k^{R(A)})^2 = \gamma \mp 2iE$. For our sample, the equation has to be solved in all three arms with correct boundary conditions at the two NS interfaces

$$\frac{\partial F}{\partial x}|_{x=\pm L_S} = \frac{\rho}{R_b} F_S|_{x=\pm L_S} \tag{7.41}$$

where ρ is the resistivity of the normal metal, R_b is the resistance times the area of the SN interface, F_S is the condensate amplitude in the bulk superconductor. The

boundary condition at the n-N interface is

$$F|_{x=L_N} = 0 \tag{7.42}$$

In addition to the continuity of F at the cross point, the conservation of the spectral supercurrent density is conserved which is equivalent to

$$\sum \partial_x F|_{x=0} = 0 \tag{7.43}$$

From these equations, we obtained the solutions for the Green's functions $\hat{F}^R = i(F_X\hat{\sigma}_X + F_Y\hat{\sigma}_Y)$ in the horizontal arm.

$$F_x = \frac{(\rho/R_b)F_S L_S}{\theta_S}\frac{\sinh(kx)}{\cosh\theta_S}\sin\frac{\phi}{2} \tag{7.44}$$

$$F_y = \frac{(\rho/R_b)F_S L_S}{\theta_S}\{\frac{(2\sinh\theta_N - \cosh\theta_N)\cosh[k(x+L_S)]}{2\sinh\theta_S\sinh\theta_N + \cosh\theta_S\cosh\theta_N} + e^{-kx}\}e^{-\theta_S}\cos\frac{\phi}{2} \tag{7.45}$$

where $\theta_{S,N} = \sqrt{(\gamma - 2iE)L_{S,N}^2/\hbar D}$ (γ is the inelastic scattering rate), and phases of the two SC reservoirs are set to $\phi/2$ and $-\phi/2$. Next, we found the values of F_x and F_y on the interface and plug them into the current (in terms of Green's function matrices) across the interface

$$I_J = -\frac{w}{16R_a}Tr\hat{\sigma}_z\int d\varepsilon[(\hat{F}^R\hat{F}_S^R - \hat{F}^A\hat{F}_S^A)(f_0 + f_{0S}) + (\hat{F}^R\hat{F}_S^A - \hat{F}^A\hat{F}_S^R)(f_0 - f_{0S})] \tag{7.46}$$

$$= -\frac{w}{16R_a}Tr\hat{\sigma}_z\int d\varepsilon[(\hat{F}^R - \hat{F}^A)(\hat{F}_S^R + \hat{F}_S^A)f_0 + (\hat{F}^R + \hat{F}^A)(\hat{F}_S^R - \hat{F}_S^A)f_{0S} \tag{7.47}$$

and

$$I_N = -\frac{\omega}{16R_a} Tr \int d\varepsilon[(\hat{G}^R - \hat{G}^A)(\hat{G}_S^R - \hat{G}_S^A) + (\hat{F}^R + \hat{F}^A)(\hat{F}_S^R + \hat{F}_S^A)](f_1 - f_{1S}) \quad (7.48)$$

In terms of F_x and F_y, the currents are written as

$$I_S = \frac{\omega}{2} Tr \int d\varepsilon\{\mathrm{Im}(F_S^R)[\mathrm{Re}(F_X^R)\cos\frac{\phi}{2} - \mathrm{Re}(F_Y^R)\sin\frac{\phi}{2}]f_0 \quad (7.49)$$

$$+ \mathrm{Re}(F_S^R)[\mathrm{Im}(F_Y^R)\sin\frac{\phi}{2} - \mathrm{Im}(F_X^R)\cos\frac{\phi}{2}]f_{0S}\} \quad (7.50)$$

$$I_N = \frac{\omega}{2} Tr \int d\varepsilon[(Re[G^R]Re[G_S^R] - (Im[F_X^R]sin\frac{\phi}{2} + Im[F_Y^R]cos\frac{\phi}{2})Im[F_S^R])f_1 \quad (7.51)$$

$f_{1S} = 0$ when the potential in that superconductor is zero. The current consists of three components discussed in chapter 5,

$$I = I_+ + I_- \cos\phi + I_C \sin\phi \quad (7.52)$$

where

$$I_\pm = \frac{1}{eR}\int_0^\infty dE\{\mathrm{Im}[F_S]\,\mathrm{Im}[\frac{F_S W_\pm}{\theta_S}]\}f_1 \quad (7.53)$$

$$I_C = \frac{1}{eR}\int_0^\infty dE\{\mathrm{Im}[F_S]\,\mathrm{Re}[\frac{F_S W_-}{\theta_S}]f_0 + \mathrm{Re}[F_S]\,\mathrm{Im}[\frac{F_S W_-}{\theta_S}]f_{0S}\} \quad (7.54)$$

and

$$W_- = \frac{\sinh\theta_N}{\theta_S(\sinh\theta_N \sinh\theta_S + 0.5\cosh\theta_N \cosh\theta_S)} \quad (7.55)$$

$$W_+ = \frac{\sinh(2\theta_S)cosh(\theta_N) + 2sinh(\theta_N)cosh(\theta_S)}{\theta_S(\sinh\theta_N \sinh\theta_S + 0.5\cosh\theta_N \cosh\theta_S)} \quad (7.56)$$

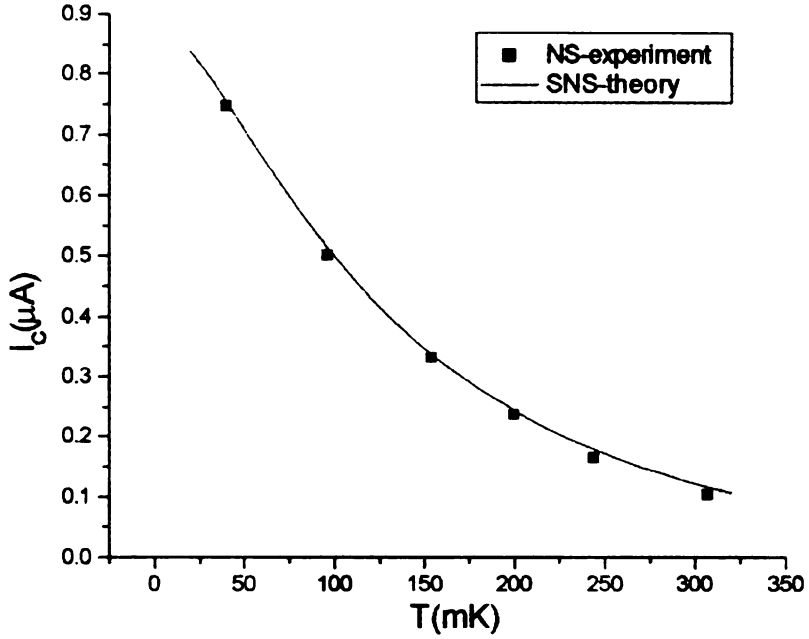

Figure 7.2: Comparison of the experiment and theory for $I_C(SNS)$ vs. T for the dangling arm case

Here, $R = 1/(G_b^2 R_N)$ where G_b is the conductance of the barrier, R_N is the resistance of the normal wire.

For the dangling arm case, we first calculated $I_C(SNS)$ vs. T. The parameters used for this calulation are $D = 120cm^2/s$, $L_S = 0.5\mu m$, $L_N = 4.5\mu m$, $\Delta = 0.191meV$, $\gamma = 0.1\Delta$, $R_N : R_b = 1 : 1$, and $R = 8\Omega$. We have found good agreement between the theory and the experiment (shown in figure 7.2.

Then, we computed $I_C(SNS)$ vs. T. We first choose the temperature points from the measurement and find the I_+, I_-, and I_C. Figure 7.4 shows the calculated results for 40 mK. $V_{critical}$ is determined by solving

$$I_+(V_{critical}) = \sqrt{I_C^2(V_{critical}) + I_-^2(V_{critical})} \tag{7.57}$$

Then, plug the $V_{critical}$ into $I_C(V_{critical})$, we obtained $I_C(SN)$ vs. T. We did not find good agreement with the experiment (shown in figure 7.3). There are two reasons for that. The first is that the scattering part of the retarded Green's function of the

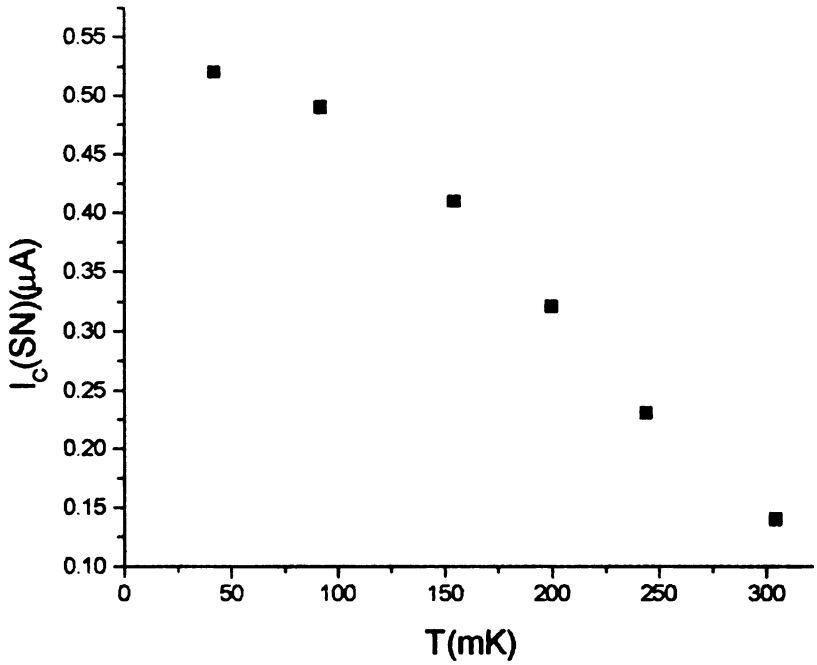

Figure 7.3: Experimental data for $I_C(SN)$ vs. T for the dangling arm case

Usadel equation becomes energy dependent when the energy of the injected quasiparticles is high. So, the solution from the equation is not correct. The other reason is that both expressions for I_+ and I_- use the equilibrium value in the normal reservoir for the antisymmetric distribution function f_1. But, f_1 can be quite different from the equilibrium value due to the presence of the long vertical arm.

For the π junction case, we first compared our numerical result and high-barrier approximation for the spectral supercurrent density $Imj(E)$. They are not very different from each other (figure 7.5). We then computed the I_C vs. V_N and compared it with the experimental result (figure 7.6). The discrepancy remains as it is in the $I_C(SN)$ vs. T calculation. We also tried computing the distribution function with Altshuler's approach plus the NS boundary conditions. It still did not improve much.

The quasiclassical approximation uses instantaneous short-range two particle interaction to treat electron-electron (ee) interaction. This may become a problem when the system is far away from equilibrium. For example, when the injected

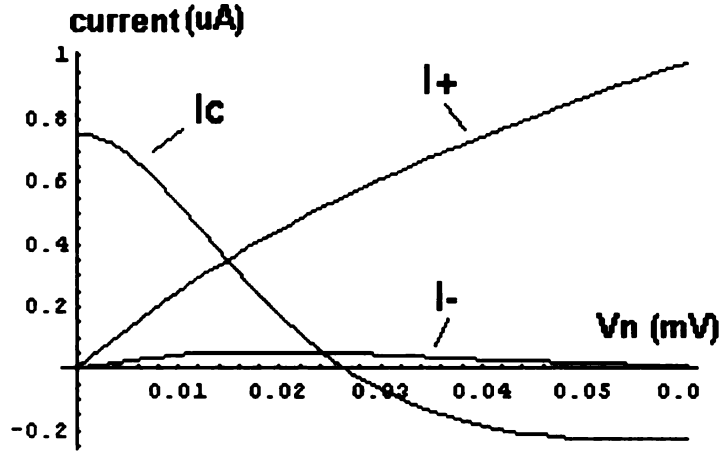

Figure 7.4: Theoretical calculations of I_+, I_-, and I_C at 40 mK

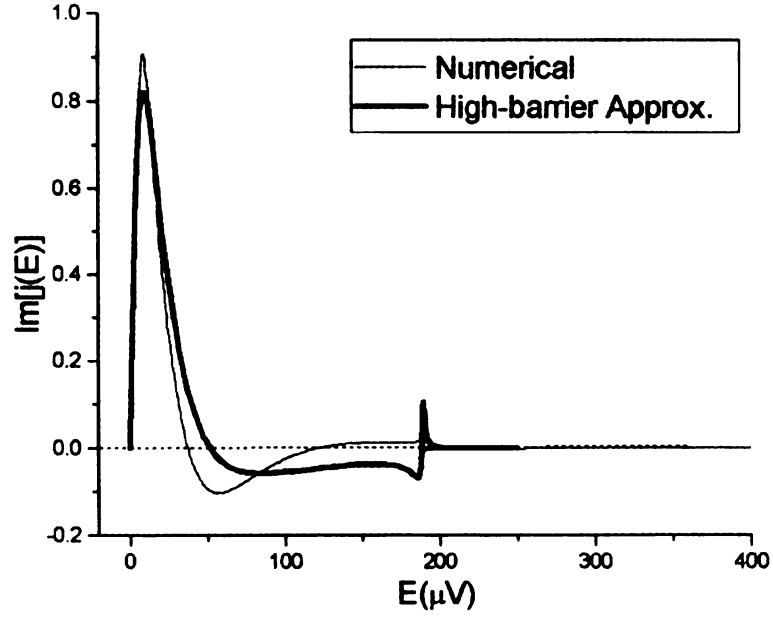

Figure 7.5: Comparison of the $Im[j(E)]$ vs. V_{inj} from the numerical calculation and the high-barrier approximation for the π junction case

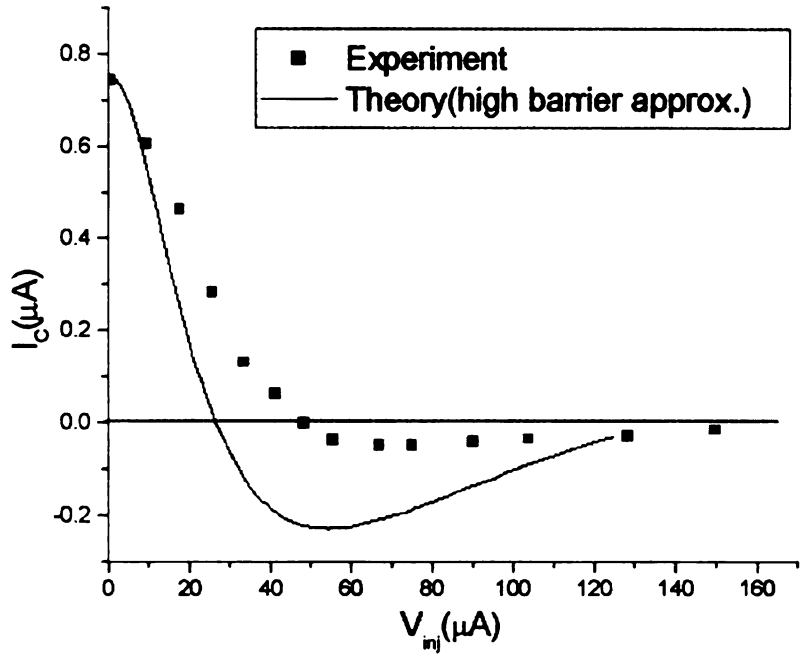

Figure 7.6: Comparison of I_C vs. V_{inj} between the theory and experiment for the π junction case

quasiparticle energy is high, the phase space opens up for ee interaction so that the electrons can no longer be treated instantaneously. So, the quasiclassical averaging is not sufficient to deal this kind of situations. The key is the correct form of the scattering part in the Usadel equation. [55] The exchange of the Green's functions must provide the right form for ee interactions. Once this is solved, we will be able to solve the transport properties by solving the Keldysh part of the Usadel equation with correct boundary conditions.

Appendices

Appendix A: Tunnel Junctions

The physical current is obtained from the Keldysh component of the Usadel equation.

$$[\check{g}_2, \check{g}_1]_K = \hat{g}_2^R \hat{g}_1 + \hat{g}_2 \hat{g}_1^A - \hat{g}_1^R \hat{g}_2 - \hat{g}_1 \hat{g}_2^A \tag{A.1}$$

where we have dropped "s". The normalization condition, $\check{g}\check{g} = 1$, allows us to choose

$$\hat{g}_{1,2} = \hat{g}_{1,2}^R \hat{f}_{1,2} - \hat{f}_{1,2} \hat{g}_{1,2}^A \tag{A.2}$$

Where the $\hat{f}$ can be taken to be diagonal (Larkin and Ovchinnikov 1975):

$$\hat{f}_{1,2} = f_{1,2}^0 \hat{\sigma}_0 + f_{1,2}^Z \hat{\sigma}_Z \tag{A.3}$$

As a result, multiplying $\hat{\sigma}_Z$ and taking the trace yields

$$j = \frac{G_T}{16e} \int_{-\infty}^{+\infty} d\epsilon \; Tr[\hat{\sigma}_Z (f_1^0 \hat{I}_a + f_2^0 \hat{I}_b + f_1^Z \hat{I}_c + f_1^Z \hat{I}_d)] \tag{A.4}$$

where

$$\hat{I}_a = [\hat{g}_2^R (\hat{g}_1^R - \hat{g}_1^A) - (\hat{g}_1^R - \hat{g}_1^A) \hat{g}_2^A]$$

$$\hat{I}_b = -[\hat{g}_1^R (\hat{g}_2^R - \hat{g}_2^A) - (\hat{g}_2^R - \hat{g}_2^A) \hat{g}_1^A]$$

$$\hat{I}_c = [\hat{g}_2^R (\hat{g}_1^R \hat{\sigma}_Z - \hat{\sigma}_Z \hat{g}_1^A) - (\hat{g}_1^R \hat{\sigma}_Z - \hat{\sigma}_Z \hat{g}_1^A) \hat{g}_2^A]$$

$$\hat{I}_d = -[\hat{g}_1^R (\hat{g}_2^R \hat{\sigma}_Z - \hat{\sigma}_Z \hat{g}_2^A) - (\hat{g}_2^R \hat{\sigma}_Z - \hat{\sigma}_Z \hat{g}_2^A) \hat{g}_1^A]$$

Due to the normalization $\check{g}^{R(A)} \check{g}^{R(A)} = 1$, we have

$$\check{g}^{R(A)} = g^{R(A)} \cdot \sigma \equiv \sum_{i=1}^{3} g_i^{R(A)} \sigma_i \tag{A.5}$$

where $g^{R(A)} = (iF^{R(A)}\sin(\phi), iiF^{R(A)}\cos(\phi), G^{R(A)})$ and ϕ is the phase of the superconducting order parameter. Hence,

$$j = \frac{G_T}{8e}\int_{-\infty}^{+\infty} d\epsilon(I_J + I_{PI}) \tag{A.6}$$

where

$$I_J = i\sin(\phi_1 - \phi_2)[f_2^0(F_2^R - F_2^A)(F_1^R + F_1^A) + f_1^0(F_2^R + F_2^A)(F_1^R - F_1^A)] \tag{A.7}$$

and

$$I_{PI} = [(G_1^R - G_1^A)(G_2^R - G_2^A) + \cos(\phi_1 - \phi_2)(F_2^R + F_2^A)(F_1^R + F_1^A)](f_1^Z - f_2^Z)] \tag{A.8}$$

I_J is the Josephson current, while I_{PI} is sometimes referred to as the quasi-particle and interference current.

Appendix B: High Barrier ($R_b >> R_N$) Approximation

Normally, one does numerical calculations because that the exact analytical result for such a problem is very difficult to obtain. Another method is to simplify the calculations with low barrier transmittance approximation.

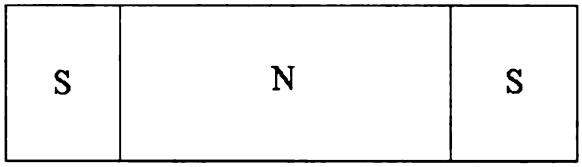

Figure B.1: SNS system

I define $r = R_b/R_N$ as the ratio of the barrier resistance and the resistance of the normal wire. The quasiclassical equation for the Green's function matrices is

$$D\ \nabla(\check{g}\nabla\check{g}) + i\varepsilon\,[\check{\sigma}_z, \check{g}] - (\gamma_N/2)\,[\check{\sigma}_z\ \check{g}\ \check{\sigma}_z,\ \check{g}] = 0 \tag{B.1}$$

Where D is the diffusion constant in the N region, and $\gamma_N = (1/2\tau_s) + Dp_s^2$ is the deparing rate. τ_s is the spin-flip scattering time and $p_s = H\lambda/\Phi_0$ is the condensate momentum due to an applied field H. The Green's functions in the superconductors and the normal metal are related through a boundary condition

$$r_b l(\check{g}\nabla\check{g})|_{\text{interface}} = [\check{g}_N, \check{g}_S] \tag{B.2}$$

Where l is the elastic mean free path. r_b is a dimensionless constant characterizing the transparency of the interface, and it is related to its resistance per unit area $R_{b\square}$ by $r_b l = 2R_{b\square}/\rho$, where ρ is the resistivity of the N region. Define a characteristic energy $\varepsilon_N = D\rho/2R_{b\square}L_N$ for describing the transmittance of the barrier. We can

rewrite equation B.1 for the advanced and retarded parts by averaging over L_N and using the boundary conditions, we obtain

$$\varepsilon_N[\hat{g}, \hat{g}_S]^{R(A)} + i\varepsilon\,[\hat{\sigma}_z, \hat{g}]^{R(A)} - (\gamma_N/2)\,[\hat{\sigma}_z\ \hat{g}\ \hat{\sigma}_z,\ \hat{g}]^{R(A)} = 0 \tag{B.3}$$

For a SNS device, it becomes

$$\varepsilon_1[\hat{g}, \hat{g}_{S1}]^{R(A)} + \varepsilon_2[\hat{g}, \hat{g}_{S2}]^{R(A)} + i\varepsilon\,[\hat{\sigma}_z, \hat{g}]^{R(A)} - (\gamma_N/2)\,[\hat{\sigma}_z\ \hat{g}\ \hat{\sigma}_z,\ \hat{g}]^{R(A)} = 0 \tag{B.4}$$

To solve this equation, we write
$\hat{g}^{R(A)} = G^{R(A)}\hat{\sigma}_z + \hat{F}^{R(A)} = G^{R(A)}\hat{\sigma}_z + (iF_x^{R(A)}\hat{\sigma}_x + iF_y^{R(A)}\hat{\sigma}_y)$, Plug into the equation above, assuming $\varepsilon_1,\ \varepsilon_2 \ll \gamma$, I obtained

$$\hat{F}^{R(A)} = \pm i(\varepsilon_1\hat{F}_{S1}^{R(A)} + \varepsilon_2\hat{F}_{S2}^{R(A)})/(\varepsilon + i\gamma) \tag{B.5}$$

where $\hat{F}_{S1}^{R(A)} = i\hat{\sigma}_y\Delta/\xi^{R(A)}$, and $\hat{F}_{S2}^{R(A)} = i(\hat{\sigma}_x\sin\phi + \hat{\sigma}_y\cos\phi)\Delta/\xi^{R(A)}$.
$\xi^{R(A)} = [(\varepsilon + i\Gamma)^2 - \Delta^2]^{1/2}$, and ϕ is the phase difference between the two superconductors one of which has zero phase. To make it easier to calculate, I assume $\varepsilon_1 = \varepsilon_2 = \varepsilon_N$. Then,

$$\hat{F}^{R(A)} = \pm\frac{i\varepsilon_N}{(\varepsilon + i\gamma)}(\hat{F}_{S1}^{R(A)} + \hat{F}_{S2}^{R(A)}) = \pm\frac{i\varepsilon_N}{(\varepsilon + i\gamma)}(i\hat{\sigma}_x\sin\phi + i\hat{\sigma}_y(1+\cos\phi))\frac{\Delta}{\xi^{R(A)}} \tag{B.6}$$

The current is obtained by plugging the solved Green's functions in the expression of the currents at the interface (written in terms of Green's function matrices)

$$I_J = -\frac{w}{16R_a}Tr\hat{\sigma}_z\int d\varepsilon[(\hat{F}^R\hat{F}_S^R - \hat{F}^A\hat{F}_S^A)(f_0 + f_{0S}) + (\hat{F}^R\hat{F}_S^A - \hat{F}^A\hat{F}_S^R)(f_0 - f_{0S})] \tag{B.7}$$

$$= -\frac{w}{16R_a}Tr\hat{\sigma}_z\int d\varepsilon[(\hat{F}^R - \hat{F}^A)(\hat{F}_S^R + \hat{F}_S^A)f_0 + (\hat{F}^R + \hat{F}^A)(\hat{F}_S^R - \hat{F}_S^A)f_{0S} \tag{B.8}$$

Appendix C: Diffusive region

The diagonal part of the Usadel equation is

$$\partial_R \hat{g}^{R(A)} \partial_R \hat{g}^{R(A)} = i\epsilon[\hat{\sigma}_Z, \hat{g}^{R(A)}] \tag{C.1}$$

and

$$\partial_R(\hat{g}^R \partial_R \hat{g} + \hat{g} \partial_R \hat{g}^A) = 0 \tag{C.2}$$

Using $\hat{g} = \hat{g}^R \hat{f} - \hat{f}\hat{g}^A$ and the equation for $\hat{g}^{R(A)}$, the equation for the Keldysh part becomes

$$\partial_R[\partial_R \hat{f} - \hat{g}^R(\partial_R \hat{f})\hat{g}^A] - (\hat{g}^R \partial_R \hat{g}^R)(\partial_R \hat{f}) - (\partial_R \hat{f})(\hat{g}^A \partial_R \hat{g}^A) = 0 \tag{C.3}$$

$\hat{f}$(the filling matrix) can be solve once $\hat{g}^R$ and $\hat{g}^A$ are determined by the diagonal part of the Usadel equation.

$$\hat{f} = f_0 \hat{\sigma}_0 + f_1 \hat{\sigma}_Z \tag{C.4}$$

In a NS system, one chooses $\hat{g}^R = G^R \hat{\sigma}_Z + iF^R \hat{\sigma}_y$ for the normal region. After multiplying by $\hat{\sigma}_Z$ and taking the trace, we have

$$\partial_R[(1 - G^R G^A - F^R F^A)\partial_R f_1] = 0 \tag{C.5}$$

These equations are no longer true if the inelastic scattering is considered. The second term is still zero after taking the trace of the product with Pauli matrix. Note, we have to multiply Pauli matrix and take trace for the Keldysh equation is because the physical current requires so. But, for the advanced and retarted equations we don't need to do this. For those we just find the Green's functions inside the normal region in terms of the Green's functions in the superconductors.

For a SNS system, the Green's function is more complicated because the phase χ varies in the normal region.

$$\hat{g}^R = G^R\hat{\sigma}_Z + iF^R(\hat{\sigma_x}sin\chi + \hat{\sigma_x}sin\chi) \tag{C.6}$$

By working out equation C.3, the total current has both supercurrent and normal current components

$$I_S = \frac{\sigma_N}{8}\int Tr\hat{\sigma}_Z(\hat{F}^R\partial\hat{F}^R - \hat{F}^A\partial\hat{F}^A)f_0 dE \tag{C.7}$$

$$I_n = \frac{\sigma_N}{8}\int Tr(1 - \hat{G}^R\hat{G}^A + \hat{F}^R\hat{F}^A)\partial f_1 dE \tag{C.8}$$

Bibliography

[1] J. J. A. Baselmans, A. F. Morpurgo, B. J. van Wees, and T. M. Klapwijk, *Reversing the direction of the supercurrent in a controllable Josephson junction*, NATURE **397**, 43 (1999).

[2] I. O. Kulik, *Macroscopic quantization and the proximity effect in S-N-S junctions*, Soviet Physics JETP **30**, 944 (19970).

[3] B. J. van Wees, K. H. Lenssen, and C. J. P. M. Harmans, *Transmission formalism for supercurrent flow in multiprobe superconductor-semiconductor-superconductor devices*, Phys. Rev. B **44**, 470 (1991).

[4] H. Pothier et al., *Energy Distribution Function of Quasiparticles in Mesoscopic Wires*, Z. Phys. **B**, 178 (1997).

[5] M. A. McCord and M. J. Rooks, *Handbook of Microlithography, Micromachining, and Microfabrication, Volume I: Microlithography*, (1999).

[6] V. Ginzburg and L. Landau, Zh. Eksperim. i Teor. Fiz. **20**, 1064 (1950).

[7] G. Deutscher and P. deGennes, *Proximity Effects*, Superconductivity edited by R.D. Parks (by Marcel Dekker, Inc.) , 1005 (1969).

[8] B. Altshuler, P. Lee, and R. A. Webb, Mesoscopic Phenomena in Solids(Amsterdam: North-Holland) (1991).

[9] V. T. Petrashov and V. N. Antonov, JETP Lett. **54**, 241 (1991).

[10] A. Kastalsky et al., *Observation of pair currents in superconductor-semiconductor contacts*, Phys. Rev. Lett. **67**, 3026 (1991).

[11] V. Ambegaokar, *Notes on review of superconductivity*, Boulder Summer School on Superconductivity (2000).

[12] L. D. Landau, Soviet Phys. JETP **3**, 920 (1957).

[13] H. Frohlich, Phys. Rev. **79**, 845 (1950).

[14] J. Bardeen, L. N. Cooper, and J. R. Schrieffer, *Theory of Superconductivity*, Phys. Rev. **108**, 1175 (1957).

[15] J. R. Schrieffer, Theory of Superconductivity (1964).

[16] G. Rickayzen, *The Theory of BCS*, Superconductivity edited by R.D. Parks (by Marcel Dekker, Inc.) , 51 (1969).

[17] M. Tinkham, Introduction To Superconductivity, second edition (1996).

[18] C. W. J. Beenakker, *Quantum transport in semiconductor-superconductor microjunctions*, Mesoscopic Quantum Physics(edited by E. Akkermans, G. Montambaux, and J. -L. Pichard) (1994).

[19] A. F. Andreev, *The thermal conductivity of the intermediate state in superconductors*, Sov. Phys. JETP **19**, 1228 (1964).

[20] G. E. Blonder, M. Tinkham, and T. M. Klapwijk, *Transition from metallic to tunneling regimes in superconducting microconstrictions: Excess current, charge imbalance, and supercurrent conversion*, Phys. Rev. B **25**, 4515 (1982).

[21] E. L. Wolf, Principle of Electron Spectroscopy, Oxford University Press (1985).

[22] S. Gueron et al., *Superconducting Proximity Effect Probed on a Mesoscopic Length Scale*, Phys. Rev. Lett. **117**, 3025 (1996).

[23] B. D. Josephson, Phys. Lett. **1**, 251 (1962).

[24] B. D. Josephson, *Weakly coupled superconductors*, Superconductivity edited by R.D. Parks (by Marcel Dekker, Inc.) , 423 (1969).

[25] S.-K. Yip, *Energy-resolved supercurrent between two superconductors*, Phys. Rev. B **58**, 5803 (1998).

[26] D. J. Thouless, *Maximum Metallic Resistance in Thin Wires*, Phys. Rev. Lett. **39**, 1167 (1977).

[27] C. Ralph and V. Ambegaokar, *Superconductivity, Andreev Reflection, and Proximity Effect in Mesoscopic Structures*, cond-mat/9709230 (1997).

[28] J. Nabity, *Menu for nanometer pattern generation system*, (1995).

[29] A. Volkov, N. Allsopp, and C. J. Lambert, J. Phys.: Condens. Matter **8**, L45 (1996).

[30] R. Shaikhaidarov et al., *Josephson effects in a superconductornormal-metal mesoscopic structure with a dangling superconducting arm*, Phys. Rev. B **62**, R14649 (2000).

[31] F. Wilhelm, *Phase-coherent transport in superconduting nanostructures*, Ph.D. Thesis (1999).

[32] A. F. Morpurgo, J. J. A. Baselmans, B. J. van Wees, and T. M. Klapwijk, *Energy Spectroscopy of Josephson Supercurrent*, J. of Low Temp. Phys. **118**, 637 (2000).

[33] M. Henny, S. Oberholzer, C. Strunk, and C. Schnenberger, *1/3-shot-noise suppression in diffusive nanowires*, Phys. Rev. B **59**, 2871 (1999).

[34] F. Pierre, *Ph.D. Thesis: Electron-Electron interactions in mesoscopic wires*, Ann. Phys. Fr. **26**, N.4 (2001).

[35] B. L. Altshuler and A. G. Aronov, Electron-Electron Interactions in Disordered Systems edited by A. L. EFROS AND M. POLLAK (North-Holland, Amsterdam) , 1 (1985).

[36] J. J. A. Baselmans, B. J. van Wees, and T. M. Klapwijk, *Nonequilibrium supercurrent transport in controllable superconductornormal-metalsuperconductor junctions*, Phys. Rev. B **63**, 094504 (2001).

[37] J. Huang et al., *Observation of a controllable π-junction in a 3-terminal Josephson device*, PRB, preparing for submission (2001).

[38] M. Octavio, M. Tinkham, G. E. Blonder, and T. M. Klapwijk, *Subharmonic energy-gap structure in superconducting constrictions*, Phys. Rev. B **27**, 6739 (1983).

[39] J. Rammer and H. Smith, *Quantum field-theoretical methods in transport theory of metals*, Rev. of Modern Phys. **52**, 323 (1986).

[40] C. Lambert and R. Raimondi, *Phase coherent transport in hybrid superconducting nanostructures*, J. Phys. Condens. Matter **10**, 901 (1998).

[41] A. L. Larkin and Y. N. Ovchinnikov, *Nonequilibrium Superconductivity edit by Langenberg and Larkin*, page 530 (1986).

[42] G. Eilenberger, *Transformation of Gorkov's equation for type-II superconductors into transpot-like equations*, Zeischrift fur Physik **214**, 195 (1968).

[43] K. D. Usadel, *Generalized Diffusion Equation for Superconducting Alloys*, Phys. Rev. Lett. **25**, 507 (1970).

[44] Y. Nambu, Phys. Rev. **117**, 648 (1960).

[45] V. Ambegaokar, *The Green's Function Method*, Superconductivity edited by R.D. Parks (by Marcel Dekker, Inc.) **I**, 259 (1969).

[46] A. L. and J. F. Walecka, Quantum Theory of Many-Particle Systems (1971).

[47] F. Zhou, B. Spivak, and A. Zyuzin, *Coherence effects in a normal-metalinsulatorsuperconductor junction*, Phys. Rev. B **52**, 4467 (1995).

[48] A. V. Zaitsev, Soviet Phys. JETP **59**, 863 (1984).

[49] F.Zhou, P.Charlat, B.Spivak, and B.Pannetier, *Density of States in Superconductor - Normal Metal - Superconductor Junctions*, J. of Low Temp. Phys. **110**, 841 (1998).

[50] A. F. Volkov, R. Seviour, and V. V. Pavlovskii, *Proximity-induced transport in hybrid mesoscopic normal-superconducting metal structures*, Superlattices and Microstructures **25**, 647 (1999).

[51] A. F. Volkov, *The proximity effect and subgap conductivity in superconductor-barrier-normal metal contacts*, Physica B **203**, 267 (1994).

[52] A. F. Volkov, *New Phenomena in Josephson SINIS Junctions*, Phys. Rev. Lett. **74**, 4730 (1995).

[53] A. F. Volkov and A. V. Zaitsev, *Phase-coherent conductance of a superconductornormal-metal quantum interferometer*, Phys. Rev. B **53**, 9267 (1996).

[54] A. V. Zaitsev, *Phase-coherent conductance of mesoscopic superconductor-normal-metal coupled systems*, Physica B **203**, 274 (1994).

[55] A. Kamenev and A. Andreev, *Electron-electron interactions in disordered metals: Keldysh formalism*, Phys. Rev. B **60**, 2218 (1999).